Article

Cell Chemical Biology

Structural Determinants for Small-Molecule Activation of Skeletal Muscle AMPK α2β2γ1 by the Glucose Importagog SC4

Graphical Abstract

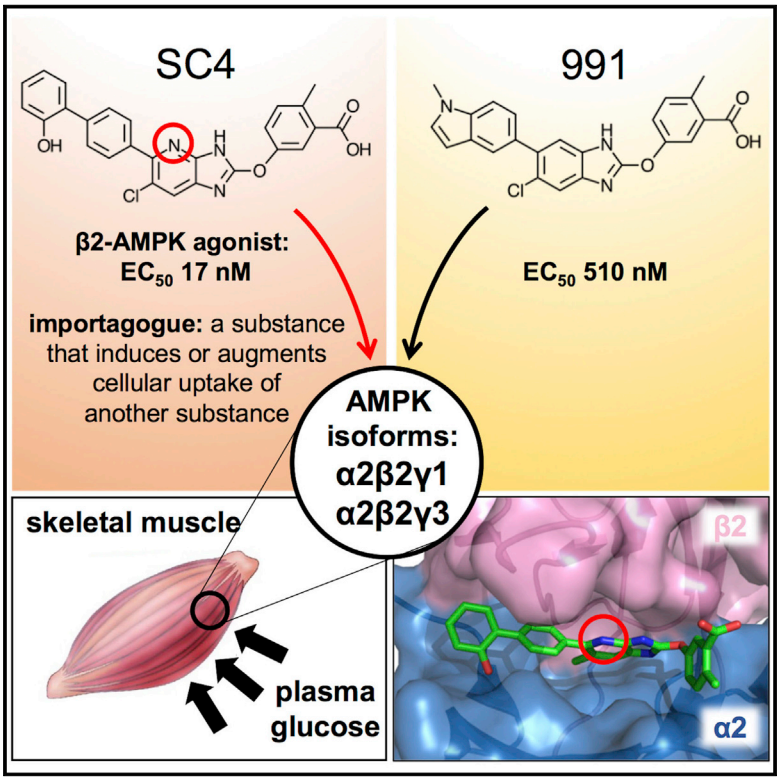

Authors

Kevin R.W. Ngoei, Christopher G. Langendorf, Naomi X.Y. Ling, ..., Bruce E. Kemp, Jonathan B. Baell, Jonathan S. Oakhill

Correspondence

clangendorf@svi.edu.au (C.G.L.), joakhill@svi.edu.au (J.S.O.)

In Brief

Therapeutic activation of the metabolic regulator AMPK in skeletal muscle is a validated strategy to combat type 2 diabetes. Ngoei et al. have solved the crystal structure of the activator SC4 complexed to a skeletal muscle AMPK isoform, identifying important binding determinants that will advance development of AMPK-targeting therapeutics.

Highlights

- SC4 is a potent allosteric activator of AMPK complexes containing the β2 isoform
- SC4 stimulates β2-AMPK in cells, and glucose uptake by isolated skeletal muscle
- Binding to β2-AMPK is mediated by 4′-nitrogen in the SC4 core and β2 residue Asp111
- We identified an interaction between β2 N terminus and AMPK autoinhibitory domain

Ngoei et al., 2018, Cell Chemical Biology *25*, 1–10
June 21, 2018
https://doi.org/10.1016/j.chembiol.2018.03.008

CellPress

Please cite this article in press as: Ngoei et al., Structural Determinants for Small-Molecule Activation of Skeletal Muscle AMPK α2β2γ1 by the Glucose Importagog SC4, Cell Chemical Biology (2018), https://doi.org/10.1016/j.chembiol.2018.03.008

Cell Chemical Biology
Article

Structural Determinants for Small-Molecule Activation of Skeletal Muscle AMPK α2β2γ1 by the Glucose Importagog SC4

Kevin R.W. Ngoei,[1,12] Christopher G. Langendorf,[1,12,*] Naomi X.Y. Ling,[2] Ashfaqul Hoque,[2] Swapna Johnson,[3] Michelle C. Camerino,[3,4] Scott R. Walker,[3,4] Ylva E. Bozikis,[3,4] Toby A. Dite,[2] Ashley J. Ovens,[2,5] William J. Smiles,[2] Roxane Jacobs,[6] He Huang,[7] Michael W. Parker,[8,9] John W. Scott,[1,5] Mark H. Rider,[6] Richard C. Foitzik,[4,10] Bruce E. Kemp,[1,5] Jonathan B. Baell,[3,11] and Jonathan S. Oakhill[2,5,13,*]

[1]Protein Chemistry & Metabolism, St. Vincent's Institute of Medical Research, University of Melbourne, Fitzroy, VIC 3065, Australia
[2]Metabolic Signalling Laboratory, St. Vincent's Institute of Medical Research, University of Melbourne, Fitzroy, VIC 3065, Australia
[3]Medicinal Chemistry, Monash Institute of Pharmaceutical Sciences, Monash University, Parkville, VIC 3052, Australia
[4]Cancer Therapeutics CRC (CTx) Pty Ltd, Level 3, 343 Royal Parade, Parkville, VIC 3052, Australia
[5]Mary MacKillop Institute for Health Research, Australian Catholic University, Melbourne, VIC 3000, Australia
[6]Université catholique de Louvain (UCL), de Duve Institute, Avenue Hippocrate 75 bte 74.02, 1200 Brussels, Belgium
[7]Jiangsu National Synergistic Innovation Center for Advanced Materials (SICAM), School of Pharmaceutical Sciences, Nanjing Tech University, No. 30 South Puzhu Road, Nanjing 211816, People's Republic of China
[8]ACRF Rational Drug Discovery Centre, St. Vincent's Institute of Medical Research, University of Melbourne, Fitzroy, VIC 3065, Australia
[9]Department of Biochemistry and Molecular Biology, Bio21 Molecular Science and Biotechnology Institute, University of Melbourne, Parkville, VIC 3052, Australia
[10]MecRX Pty Ltd, Level 9, 31 Queen Street, Melbourne, VIC 3000, Australia
[11]School of Pharmaceutical Sciences, Nanjing Tech University, No. 30 South Puzhu Road, Nanjing 211816, People's Republic of China
[12]These authors contributed equally
[13]Lead Contact
*Correspondence: clangendorf@svi.edu.au (C.G.L.), joakhill@svi.edu.au (J.S.O.)
https://doi.org/10.1016/j.chembiol.2018.03.008

SUMMARY

The AMP-activated protein kinase (AMPK) αβγ heterotrimer regulates cellular energy homeostasis with tissue-specific isoform distribution. Small-molecule activation of skeletal muscle α2β2 AMPK complexes may prove a valuable treatment strategy for type 2 diabetes and insulin resistance. Herein, we report the small-molecule SC4 is a potent, direct AMPK activator that preferentially activates α2 complexes and stimulates skeletal muscle glucose uptake. In parallel with the term secretagog, we propose "importagog" to define a substance that induces or augments cellular uptake of another substance. Three-dimensional structures of the glucose importagog SC4 bound to activated α2β2γ1 and α2β1γ1 complexes reveal binding determinants, in particular a key interaction between the SC4 imidazopyridine 4′-nitrogen and β2-Asp111, which provide a design paradigm for β2-AMPK therapeutics. The α2β2γ1/SC4 structure reveals an interaction between a β2 N-terminal α helix and the α2 autoinhibitory domain. Our results provide a structure-function guide to accelerate development of potent, but importantly tissue-specific, β2-AMPK therapeutics.

INTRODUCTION

Type 2 diabetes (T2D) is a progressive disease, characterized in its early stages by varying degrees of pancreatic β cell dysfunction and insulin resistance. Insulin secretagogs (Greek *agōgos*; leading), such as the sulfonylureas (SUs) and glinides, which stimulate insulin secretion from remaining functional β cells, are widely used to overcome initial decline in production (Hanefeld, 2007; Carpio and Fonseca, 2014; Thrasher, 2017). However, chronic SU use is associated with β cell apoptosis, exhaustion, and desensitization, and retention of glycemic control over time usually requires progression to combinatorial therapy. Other complications, including weight gain, cardiotoxicity, and hypoglycemia, warrant the continued development of therapies with alternative modes of action to SUs. Peripheral insulin sensitization by the thiazolidinediones (TZDs), for example, is one such successful strategy. Another emerging strategy for glycemic control, underpinned by its implicated roles in exercise-induced glucose clearance, is targeting of AMP-activated protein kinase (AMPK) to promote glucose disposal and storage in skeletal muscle (O'Neill, 2013; Cokorinos et al., 2017; Myers et al., 2017).

AMPK is a myristoylated αβγ heterotrimer that plays an important role in regulating metabolism in eukaryotes by balancing nutrient supply with energy demand (reviewed in Hardie, 2015; Oakhill et al., 2012). Elevations in cellular AMP/ATP and ADP/ATP ratios, induced by energy stress, are detected by AMPK and promote phosphorylation of the AMPK catalytic α-subunit

activation loop residue T172 (α-pT172) by LKB1 and CaMKK2, triggering the AMPK signaling cascade. Current models of allosteric regulation depict exchange of ATP for AMP at binding sites in the γ subunit, leading to sequestration of a tri-helical autoinhibitory domain (AID) located immediately C-terminal to the catalytic kinase domain (Chen et al., 2013). AMPK acts to restore cellular energy balance through phosphorylation of numerous key metabolic enzymes, resulting in inhibition of ATP-consuming anabolic pathways and promotion of ATP-generating catabolic processes.

The potential of AMPK drugs has been pre-clinically validated by recent and extensive *in vivo* characterization of high-potency pan-AMPK activators PF-739 (Cokorinos et al., 2017) and MK-8722 (Myers et al., 2017). Uniquely, these drugs induced robust, skeletal muscle AMPK-dependent glucose disposal, and improved glucose homeostasis, in diabetic mice and non-human primates, both important attributes for T2D therapeutics. With MK-8722, however, chronic dosing was associated with cardiac related complications (glycogen accumulation and hypertrophy) reminiscent of chronic AMPK activation (Hardie, 2014), potentially compromising the therapeutic use of these pan-AMPK activators in a clinical setting.

Mammalian AMPK consists of a catalytic α subunit and regulatory β and γ subunits. The β subunit is myristoylated at position Gly2, a modification important for spatiotemporal regulation of AMPK signaling (Oakhill et al., 2010; Zhang et al., 2017). Each subunit has multiple isoforms (α1, α2, β1, β2, γ1, γ2, γ3) that are differentially expressed and regulated throughout the human body. For example, α1- and α2-AMPK complexes contribute similarly to total AMPK activity in the human heart (Kim et al., 2012), whereas α2 and β2 are highly expressed, and almost exclusively associated, in human skeletal muscle (Thornton et al., 1998; Cheung et al., 2000; Wojtaszewski et al., 2005). Since skeletal muscle is the primary organ for glucose disposal and storage, and β2-AMPK has an established role as a driver of insulin-independent skeletal muscle glucose clearance (Scott et al., 2008), α2β2 complexes are regarded as important drug targets to treat metabolic diseases, in particular T2D. However, first-generation direct-acting AMPK drugs (e.g., A769662, salicylate, PF-06409577, and, to a lesser extent, 991), show strong β1-isoform selectivity (Cool et al., 2006; Scott et al., 2008; Hawley et al., 2012; Cameron et al., 2016; Xiao et al., 2013). All these AMPK drugs likely occupy a pocket formed between the β-subunit carbohydrate binding module (CBM, β1 residues 76–156) and the N-terminal lobe of the α-subunit kinase domain (Xiao et al., 2013; Calabrese et al., 2014) (termed the ADaM [allosteric drug and metabolite] site [Langendorf and Kemp, 2015]). This pocket is stabilized in the β1 isoform by phosphorylation of the CBM residue S108, which sensitizes β1-AMPK to ADaM-site agonists and may play a role in pro-survival pathways (Dite et al., 2017). Furthermore, β1-pS108 renders phosphorylation of α-T172 dispensable for activation by ADaM-site drugs, whereas unphosphorylated AMPK remains sensitive to synergistic activation in the presence of both AMP and ADaM-site drugs (Scott et al., 2014; Dite et al., 2017).

Despite their demonstrated applicability, structural information relating to how drugs bind to, and activate, β2-AMPK is lacking; this represents a major obstacle to drug development efforts. PF-739 was co-crystallized with the α1β1γ1 complex, whereas the only previous structures of the β2-AMPK heterotrimer captured the analogous ADaM site in the apo form, and consequently was not informative on the binding determinants important for drug action (Li et al., 2015). In this study, we describe the first crystal structures of phosphorylated α1β2γ1 and α2β2γ1 with an occupied ADaM site. Crystallization was aided by inclusion of the potent, small-molecule β2-AMPK activator SC4, and comparative structural analysis reveals the β2-specific residue D111 as a key mediator of drug activation. We consider that the results provide a structure-function guide to accelerate development of more potent, but importantly tissue-specific, β2-AMPK therapeutics.

RESULTS

SC4 Is a Potent Activator of α2β2-AMPK Complexes

To expand the repertoire of fully characterized β2-AMPK agonists, we selected and synthesized the small-molecule SC4 from the patent literature (Tonogaki et al., 2013) (Figure 1A). Structurally, SC4 shares the ring-3 (2-methylbenzoic acid/*o*-toluic acid) and core ring-2 (imidazopyridine) groups with 991, but differs in the presence of a nitrogen atom at the 4′ position. When screened against all 12 AMPK heterotrimeric combinations (Table S1), SC4 activated complexes containing either β isoform, but at 0.5 μM displayed a selectivity preference for AMPK α2 (all six α2 complexes were significantly activated, compared with two [α1β1γ1 and α1β1γ3] out of six α1 complexes) (Figure 1B and Table S2). Importantly, SC4 significantly activated α2β2γ1 (EC_{50} 17.2 ± 1.6 nM) and α2β2γ3 (EC_{50} 82.1 ± 1.3 nM), the predominant AMPK isoform complexes in human skeletal muscle (Wojtaszewski et al., 2005), but ≤5 μM failed to significantly stimulate activities of the α1-equivalent complexes, α1β2γ1 and α1β2γ3 (Figure 1C).

We performed further biochemical analyses to determine the mechanism of β2 activation by SC4. Deletion of the β-subunit CBM in both AMPK α2β1γ1 and α2β2γ1 abolished SC4 activation, whereas AMP activation was largely preserved (Figure S1A). This strongly indicates that SC4 occupies a pocket in α2β2γ1 analogous to the ADaM site in β1-AMPK complexes. Exchange of the phosphorylation site β-S108 for Ala increased the SC4 activation EC_{50} by ~4-fold for both α2β2γ1 and α2β1γ1, without significantly altering maximal activation (Figure S1B and Table S2). This is in contrast to A-769662, which has an absolute requirement for S108 phosphorylation to activate β1-AMPK, but broadly in line with similar experiments conducted with 991 (Willows et al., 2017a). As previously shown with A-769662 (Scott et al., 2014), SC4 synergistically activated dephosphorylated α1β1γ1 in the presence of AMP (>500-fold activation); however, AMP/drug synergistic activation did not translate to the α2β2γ1 isoform complex (Figure S1C).

SC4 Triggers AMPK Cellular Signaling

We investigated SC4 cellular bioactivity in differentiated C2C12 myotubes that express α2β2γ3 (Bultot et al., 2016). Incubation of these cells with SC4 induced dose-dependent increases in phosphorylation of the AMPK protein substrate

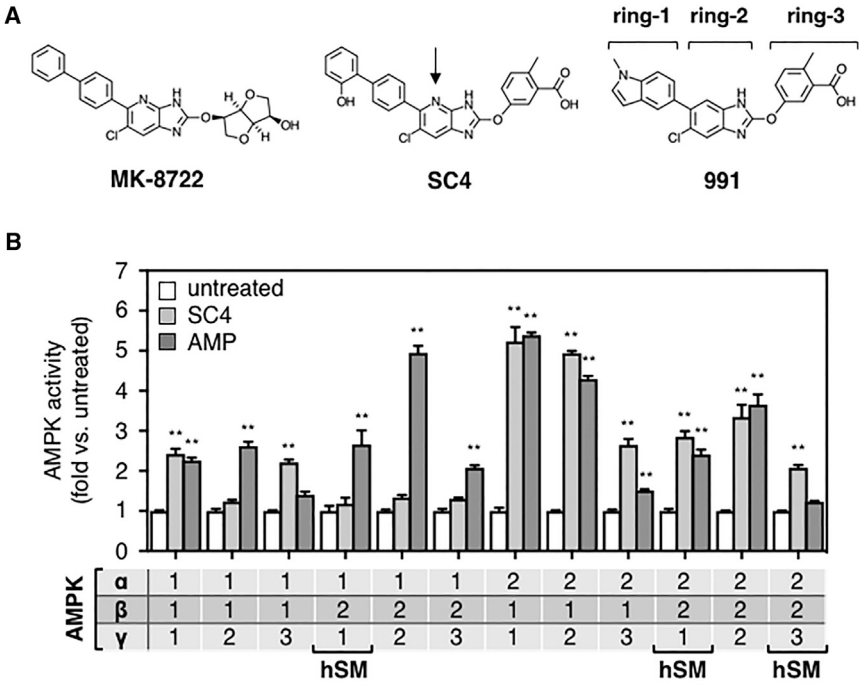

Figure 1. Biochemical Analysis of SC4

(A) Structures of MK-8722, SC4, and 991. Arrow indicates SC4 4′-nitrogen.

(B) Regulation of human AMPK isoforms by SC4. Twelve AMPK heterotrimeric combinations, as indicated, were purified from COS7 mammalian cells and activities measured in the presence of SC4 (0.5 μM) or AMP (100 μM). n = 4, data presented as mean AMPK activity (fold change relative to untreated ± SEM). Basal activities for each isoform are displayed in Table S1. Statistical analysis was performed using two-way ANOVA with post hoc Dunnett's multiple comparison test. **$p < 0.01$ indicates significant increase in activity relative to untreated. hSM denotes isoforms previously detected in human *vastus lateralis* muscle (α2β2γ1 > α2β2γ3 = α1β2γ1) (Wojtaszewski et al., 2005).

(C) Dose-response curves for SC4 (0–5 μM) activation of AMPK isoforms α2β2γ1, α2β2γ3, α1β2γ1, and α1β2γ3. n = 4, data presented as mean AMPK activity (fold change relative to untreated ± SEM). Isoform-specific EC_{50} values for SC4 and 991 (Xiao et al., 2013) are displayed in the associated table. See also Figure S1; Tables S1 and S2.

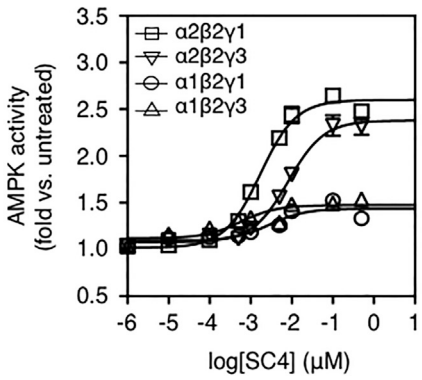

AMPK	EC_{50} (nM ± s.e.m.)	
	SC4	991
α2β2γ1	17.2 ± 1.6	510 ± 190
α2β2γ3	82.1 ± 1.3	n.d.

acetyl-coenzyme A carboxylase (ACC) (Figures 2A and S2A). A similar effect on AMPK signaling was seen in primary mouse hepatocytes that predominantly express β1-AMPK (Stephenne et al., 2011) (Figure S2B). In both cell types, SC4-induced AMPK signaling was not accompanied by changes in either AMPK pT172 or AMP/ATP ratio (Figures 2A and 2B [C2C12 myotubes] and Figures S2B and S2C [hepatocytes]), indicating that SC4 acts directly on AMPK. This is in contrast to the mitochondrial complex 1 inhibitor phenformin, which indirectly triggers T172 phosphorylation and AMPK signaling by elevating intracellular AMP levels (Figures 2A and 2B [C2C12 myotubes] and Figures S2B and S2C [hepatocytes]). MK-8722 (>1 μM) and 991 (10 μM) also induced phosphorylation of T172 in hepatocytes and C2C12 myotubes, respectively (Myers et al., 2017; Bultot et al., 2016), although their effects on adenine nucleotide ratios were not measured. To unambiguously demonstrate cellular SC4 activation of β2-AMPK, we used a lentiviral system to re-introduce the β2 subunit into an immortalized mouse embryonic fibroblast (iMEF) cell line genetically deficient in AMPK β1 and β2 (β1/β2 double-knockout [dKO] iMEFs) (Dite et al., 2017). This was sufficient to reconstitute AMPK heterotrimer expression and signaling (Figure 2C). Incubation of these "β2-AMPK only" iMEFs with 1 μM SC4 induced a significant increase in phosphorylation of ACC S79 without altering pT172 (Figure 2D). At 10 μM SC4 treatment, however, ACC S79 phosphorylation was associated with an increase in T172 phosphorylation. Combined, SC4 allosterically activates AMPK in diverse cellular contexts, without relying on changes in AMP/ATP ratio or pT172.

SC4 Stimulates Skeletal Muscle Glucose Uptake

AMPK-mediated glucose uptake by skeletal muscle is a validated therapeutic approach to improve glucose homeostasis *in vivo* (Cokorinos et al., 2017; Myers et al., 2017). Indeed, SC4 pre-incubation caused a significant increase in 2-deoxyglucose transport into both isolated *soleus* and *extensor digitorum longus* (EDL) muscles from wild-type (WT), but not β2-KO, mice (Figures 3A and S3). In mouse *epitrochlearis* muscle *ex vivo*, SC4 (1 μM and 2 μM) acted synergistically with low-frequency electrical

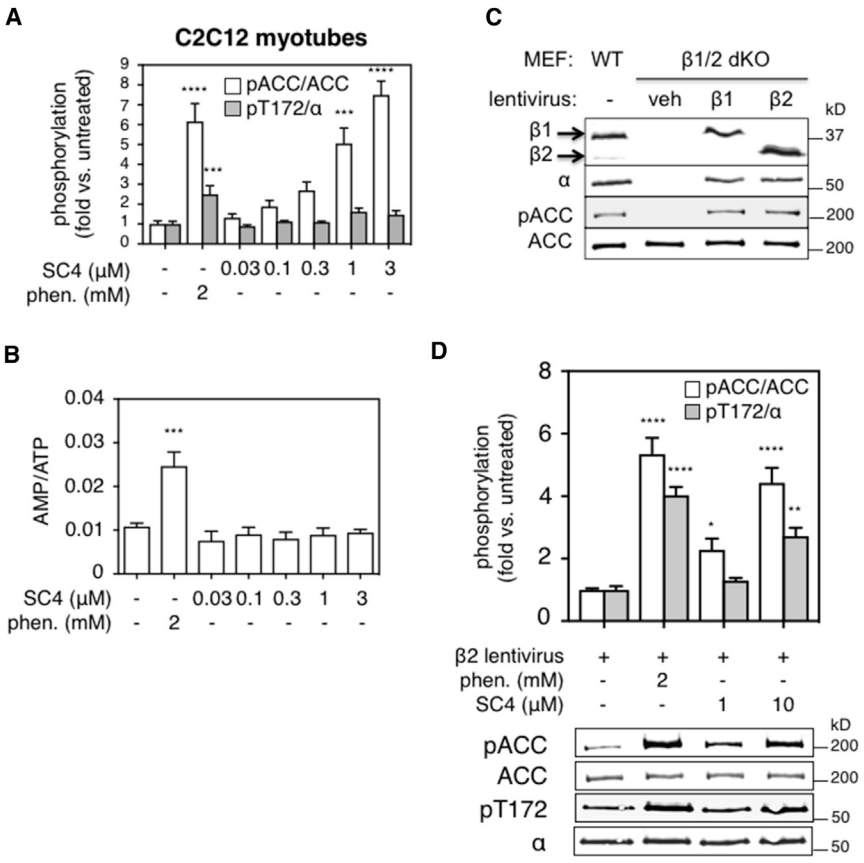

Figure 2. SC4 Cellular Bioactivity

(A) Differentiated C2C12 myoblasts were incubated with phenformin (2 mM) or SC4 (as indicated). Prepared lysates were assessed for phosphorylation of ACC (pACC) and AMPK α-T172 (pT172) by immunoblot. n = 4, data presented as mean phosphorylation (fold change relative to untreated ± SEM). Representative immunoblots in Figure S2A. Statistical analysis was performed by one-way ANOVA with post hoc Dunnett's multiple comparison test. ***p < 0.001 and ****p < 0.0001 indicate significant increase in phosphorylation relative to untreated.

(B) Adenine nucleotides were extracted from treated C2C12 myoblasts with perchloric acid, and relative concentrations measured by mass spectrometry. n = 3, data presented as mean AMP/ATP ratio ± SEM. Statistical analysis was performed by one-way ANOVA with post hoc Dunnett's multiple comparison test. ***p < 0.001 indicates significant increase in AMP/ATP ratio relative to untreated.

(C) Lentiviral expression of β1 or β2 isoforms in AMPK β1/2 double-knockout immortalized mouse embryonic fibroblasts (β1/2 dKO iMEFs) reconstitutes AMPK heterotrimer expression and signaling. Lysates prepared from WT iMEFs, or β1/2 dKO iMEFs transduced with empty virus (veh), or FLAG-fusions for either β1 or β2 isoform, were analyzed by immunoblot as indicated.

(D) β2-expressing β1/2 dKO iMEFs were incubated with phenformin (2 mM) or SC4 (as indicated). Prepared lysates were assessed for phosphorylation of ACC (pACC) and AMPK α-T172 (pT172), relative to total protein, by immunoblot. n = 3, data presented as mean phosphorylation (fold change relative to untreated ± SEM). Representative immunoblots are shown. Statistical analysis was performed by one-way ANOVA with post hoc Dunnett's multiple comparison test. *p < 0.05, **p < 0.01, and ****p < 0.0001 indicate significant increase in phosphorylation relative to untreated.

See also Figure S2.

stimulation to induce phosphorylation of ACC to levels comparable with that seen with 5 μM 991 and electrical stimulation (Figure 3B).

Structural Characterization of SC4 Binding to α2β2γ1

With these demonstrated bioactive properties, we regard SC4 as an excellent model compound to aid future AMPK drug design. For this purpose we solved the co-crystal structures of SC4 complexed to full-length AMPK α2β2γ1 and α2β1γ1 heterotrimers phosphorylated at T172 and S108 (p-α2β2γ1 and p-α2β1γ1, respectively) (Table S3). These represent the first crystal structures of a drug bound to the therapeutically important α2/β2-isoform combination that is found enriched in human skeletal muscle. Consistent with our biochemical characterization (Figure S1), SC4 is clearly visible bound to the region in β2 equivalent to the ADaM site in β1 (Figures 4A and S4A–S4C). Unambiguous density exists for the β-subunit C-interacting helix in both structures, and these overlay well. Critically, the structures show the kinase small-lobe C helices aligned in an active orientation, and in the high-resolution α2β1γ1 structure the αE64-αK45 salt bridge is intact, again indicative of the active AMPK conformation (Taylor et al., 1993). Comparison of the p-α2β2γ1/SC4 structure and the previously solved PF-739, PF-06409577, and 991 co-crystal complexes (Cokorinos et al., 2017; Cameron et al., 2016; Xiao et al., 2013) indicates a conserved manner of binding (Figure S4D). Using the high-resolution SC4-bound p-α2β1γ1 structure, we reveal that these compounds are well aligned at the hydrophobic channel that houses ring-1 elements, and at the hetero-ring-2 fused cores, with the critical α2- and β1-interacting residues maintaining a similar conformation for all four compounds, despite their structural differences (Figure 4B). In one SC4-bound heterotrimer (heterotrimer A), the *o*-toluic acid ring-3 has been modeled in two conformations (Figure S4B), suggesting that this group is flexible. In the alternative SC4-bound heterotrimer (heterotrimer B) the *o*-toluic acid group is modeled in one distinct conformation; however, there is a ring-to-ring π-stacking interaction between ring-3 of SC4 and an imidazole molecule from the crystallization experiment (Figure S4C). This imidazole makes a further ring-to-ring π-stacking interaction with α2-F27, which has an altered conformation to participate in the interaction.

β2-D111 Is Critical for SC4 β2-AMPK Activation

These structural data indicate that the β2-CBM can function almost identically to the β1-CBM with respect to ADaM-site allosteric activation of AMPK; hence we reason that the β-isoform specificity of ADaM-site activators is more likely due to specific residues and not the overall CBM/kinase N-lobe conformation. Compared with the β1/SC4 structure, SC4 bound to β2 makes an additional salt-bridge interaction between the

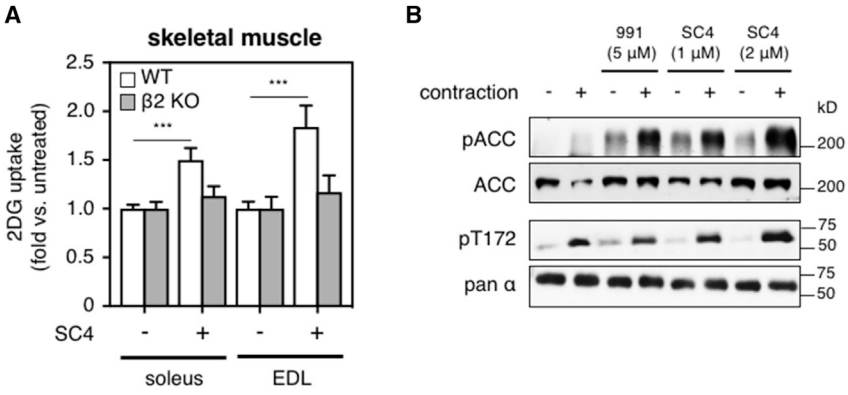

Figure 3. SC4 Bioactivity in Skeletal Muscle

(A) *Soleus* and *extensor digitorum longus* (EDL) muscles, isolated from AMPK WT and β2 KO mice, were pre-incubated ± SC4 (10 μM) and measured for 2-deoxyglucose (2DG) uptake. n = 3–12, data presented as mean 2DG uptake (fold increase relative to untreated ± SEM). Statistical analysis for muscle incubations was performed by unpaired two-tailed Student's t test. ***$p < 0.001$ indicates significant increase in 2DG uptake relative to WT untreated.

(B) *Epitrochlearis* muscles were isolated from WT mice and incubated with/without 991 (5 μM) or SC4 (1 μM or 2 μM), with or without contraction induced by electrical stimulation. Prepared lysates were assessed for pACC and AMPK α-pT172 by immunoblot. A representative immunoblot from 5–6 independent experiments is shown.

See also Figure S3.

non-conserved CBM residue β2-D111 and the 4′-nitrogen in the imidazopyridine ring-2 of the SC4 core (Figures 1A and 4C). β2-D111 makes another interaction with β2-R82, which forms a cationic π-stacking interaction with SC4 ring-2, similar to previous β1-R83 drug-bound structures (Figures 4B and 4C). We speculated that the β2-D111-SC4 core interaction may account for the increased β2 potency of SC4, relative to 991. Indeed, mutation of β2-D111 to Ala resulted in almost total loss of SC4 activation, whereas mutation of the analogous β1 residue N111 to Ala had a less dramatic effect, increasing EC_{50} only ~3-fold (Figure 4D and Table S2). Conversely, substitution of the SC4 4′-nitrogen for carbon (cSC4) resulted in ~6-fold reduction in potency for α2β2γ1 AMPK (EC_{50}: 16.3–99.2 nM) (Figure 4E).

A β2-Subunit α Helix Interacts with the Autoinhibitory Domain of α2

We detected unique electron density in the p-α2β2γ1/SC4 complex that had not been seen in earlier AMPK structures. Despite medium resolution, this enabled us to model main-chain density for extra residues N-terminal to the CBM Pro78 in the only other available β2-AMPK structure (Li et al., 2015). The most striking element of this extended structure is a short α helix, which we have assigned as comprising β2 residues Phe60 to Ser70, positioned within a shallow, open groove bordered by the three helices constituting the α2 AID (Figures 5A–5C). This groove is apparent, yet vacant, in other AMP-bound AMPK structures with a resolved AID (e.g., PDB: 4RER and 5IS0) (Figure 5C), and in our p-α2β1γ1/SC4 complex (Figure 5D), but is largely inaccessible in isolated human α2 AID (PDB: 2LTU) or inactive kinase domain AID (PDB: 4RED) structures due to inward rotations of α helices 1 and 2 (Figure 5E). Consistent with the active-state structures, the AID in our p-α2β2γ1/SC4 complex is sequestered away from the kinase domain small lobe, and rotated by ~180° such that the kinase domain-interacting surface now faces the γ subunit CBS2. However, interaction with the β2 α helix in our structure results in an additional rotation, centered around the C-terminal end of the AID α helix 3, culminating in a further 11-Å shift in AID α helices 1 and 2 toward the γ subunit CBS2 (Figure 5F).

To investigate the significance of the β2/AID interaction for AMP or SC4 regulation, we expressed a truncated AMPK complex (α2β2ΔNtermγ1) with the N-terminal 68 residues of the β2 subunit deleted. We were unable to obtain sufficient expression of the truncated heterotrimer in mammalian cells; therefore we used our *Escherichia coli* expression system and activated WT and β2ΔNterm complexes during purification by CaMKK2-mediated phosphorylation of T172 (Figure 5G). SC4 activated both AMPK complexes with similar potencies (p-α2β2γ1 EC_{50} 68.8 ± 1.1 nM, p-α2β2ΔNtermγ1 EC_{50} 31.4 ± 1.1 nM) and maximal fold activations (Figure 5H). Similarly, 100 μM AMP activated both AMPK complexes by a similar magnitude.

DISCUSSION

The insulin-sensitizing and glucose-disposing properties of AMPK activation in skeletal muscle in response to physical exercise/contraction are well established and remain intact in individuals with T2D (Kjøbsted et al., 2016). Therefore, it is of little surprise that small-molecule activation of AMPK in this tissue is remarkably effective at lowering serum glucose levels and improving glucose homeostasis in animal models of diabetes (Cokorinos et al., 2017; Myers et al., 2017). A similar strategy may be usefully employed to treat T2D in humans, given consistent AMPK isoform expression in skeletal muscle across mammalian species. Importantly, these pan-AMPK activators did not induce hypoglycemia, and exerted glycemic control independently of increased insulin levels. This provides them with an important and unique advantage over current, incretin-based therapeutics (e.g., SUs), chronic use of which has been associated with pancreatic β cell exhaustion, desensitization, and apoptosis (Hanefeld, 2007). Substances that cause or promote secretion of another substance, e.g., SUs (pancreatic insulin secretion) and ghrelin (growth hormone release from the hypothalamus), are collectively termed secretagogs. A comparative term for induced augmentation of cellular import does not currently exist, thus we propose "importagog" to describe a substance or compound that causes or promotes import or uptake of another substance into a cell or tissue. Accordingly, insulin, TZDs, and other synthetic drugs with glucose-lowering actions can be classified as glucose importagogs.

In the current study we first describe structural characterization of the drug binding site in human skeletal muscle AMPK α2β2γ1. Success in AMPK crystallization was provided by

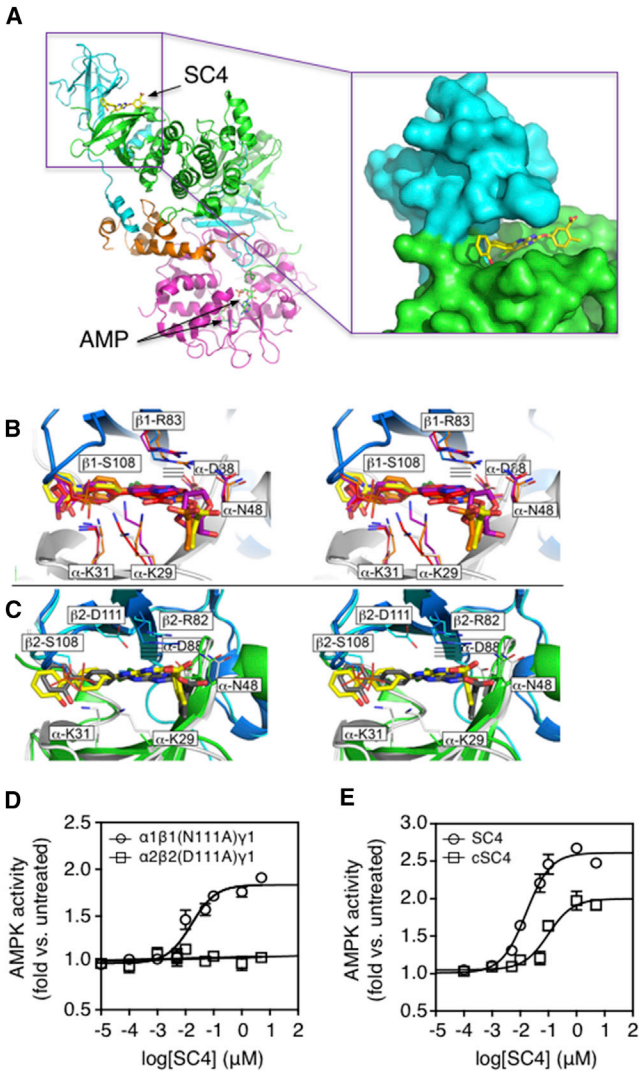

Figure 4. SC4 Occupies the β2-ADaM Site

(A) Cartoon representation of full-length p-α2β2γ1 (α2, green; β1, cyan; γ1, magenta) in complex with SC4 and two AMP molecules (γ sites 3 and 4). Inset: surface representation centered on SC4 bound in the β2-ADaM site, formed between the N lobe of the α-kinase domain and β2-CBM.

(B) Stereo view of the SC4-occupied ADaM site in p-α2β1γ1 AMPK (α2, white; β1, blue), superposed with compounds 991 (PDB: 4CFE, orange), PF-739 (PDB: 5UFU, purple), and PF-06409577 (PDB: 5KQ5, red), and their respective interacting residues. Interacting residues (color matched with compound) occupy a similar conformation, suggesting a common interaction profile for all compounds shown. β1-S108 is phosphorylated in 4CFE; phosphomimetic β1-D108 is used in 5UFU and 5KQ5.

(C–E) Stereo view of p-α2β2γ1 (α2, white; β2, light blue) and p-α2β1γ1 (α2, green; β1, dark blue) superposed to highlight the conformational changes in β1/2 residue interactions with SC4 (yellow and gray, respectively). The side-chain oxygen of the non-conserved residue β2-D111 is favorably positioned to form an interaction with the SC4 4′-nitrogen and β2-R82. Some β2 side chains have not been modeled due to poor electron density. Dose-response curves for (D) SC4 (0–5 μM) activation of AMPK mutants α1β1(N111A)γ1 and α2β2(D111A)γ1, and (E) cSC4 (0–5 μM) activation of α2β2γ1. AMPK complexes were purified from COS7 mammalian cells. n = 4, data presented as mean AMPK activity (fold change relative to untreated ± SEM).

See Figure S4; Tables S2 and S3.

addition of the nanomolar affinity β2-AMPK activator SC4, the fourth member of a class of drugs demonstrated to promote insulin-independent skeletal muscle glucose uptake *in vivo* (PF-739 and MK-8722) or *ex vivo* (991 and SC4). SC4 triggered AMPK signaling in a range of cell types by a purely allosteric mechanism, and in doing so acted independently of changes to intracellular AMP/ATP ratio or pT172. This disconnect between pT172 levels and AMPK activation by SC4 mirrors previous observations using A-769662 (Scott et al., 2014) and MK-8722 (Myers et al., 2017). Similarly, SC4-stimulated glucose uptake in isolated mouse *soleus*, EDL, and *epitrochlearis* muscles was not accompanied by detectable elevations in pT172. Combined, these studies reinforce our view that pT172 in isolation should not be regarded as a definitive measure of cellular AMPK activity, particularly in response to drug treatment.

We recently showed that, when co-incubated with A-769662 and phenformin, significant pT172-independent α2-AMPK signaling could be detected in $\alpha1^{-/-}/\alpha2^{-/-}$ MEFs exclusively expressing T172A-mutated α2 complexes (Dite et al., 2017); this despite the generally smaller magnitude of AMP/A-769662 dual-ligand co-activation of α2 complexes compared with α1 (Langendorf et al., 2016). In contrast, treatment of A549 cells, lacking LKB1 and genetically deleted for CaMKK2, with 2-deoxyglucose (2DG, mimicking glucose starvation) and 991 failed to stimulate T172 phosphorylation and only modestly induced AMPK activity (Willows et al., 2017b). The reason for this discrepancy is unclear, although we note that 991 poorly activated dephosphorylated, purified α1β1γ1 in the presence of AMP (117-fold) compared with A-769662 (>1,000-fold) (Scott et al., 2014), possibly accounting for the weaker cellular response. Alternatively, AMP/drug (or AMP/metabolite) activation of dephosphorylated AMPK may be cell specific (governed by α1/α2 expression ratio) and highly contextual in that individual energy stresses (e.g., glucose starvation versus inhibition of mitochondrial function) give rise to distinct effects. Willows et al. (2017b) raise the argument that, because activities achieved by dual-liganded, unphosphorylated AMPK are low (~10%) relative to that obtained following stoichiometric (100%) CaMKK2 phosphorylation, physiological relevance of this mechanism as a means for AMPK regulatory control remains doubtful. We note that in the same study the measured stoichiometry of cellular pT172 following 2DG treatment, which induced a substantial increase in ADP/ATP ratio, was at maximal 10%. This is consistent with our own observations in COS7 cells, in which pT172 levels reached ~8% following treatment with ionomycin, a Ca^{2+} ionophore and CaMKK2 activator, and rapidly returned to basal levels following removal of the stimulus (Scott et al., 2014). Thus, pT172 is tightly constrained by strong phosphatase(s) pressure and is unlikely to reach high stoichiometry, even during periods of extreme cellular stress. We therefore argue that dual-ligand activation of unphosphorylated AMPK, which represents the major form of cellular AMPK and is of course free from phosphatase regulation, represents a relevant magnitude of AMPK activation.

SC4, despite being a potent activator of p-α2β2γ1, was unable to activate dephosphorylated α2β2γ1 in the presence of AMP (Figure S1C). Comparison of two crystal structures of the α2β1γ1/AMP/991 complex reveal that the activation loop

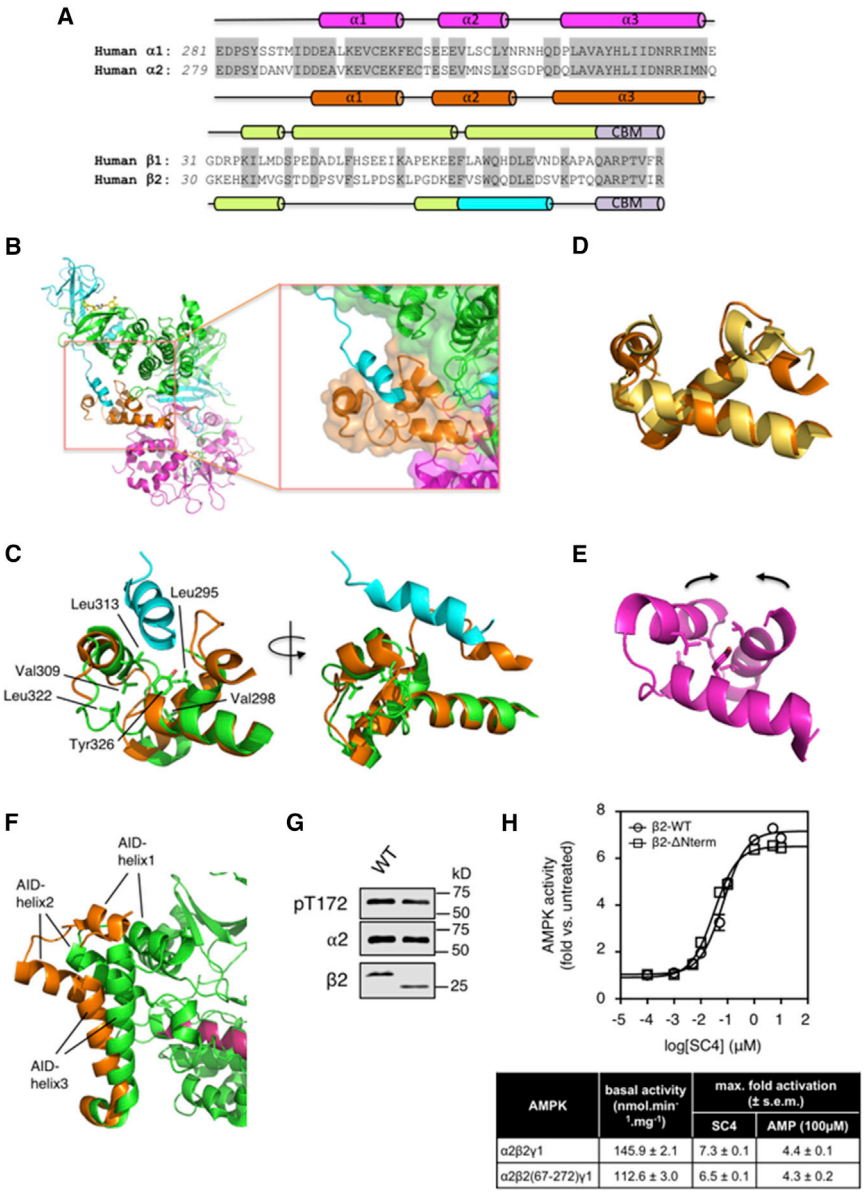

AMPK	basal activity (nmol.min^{-1}.mg^{-1})	max. fold activation (± s.e.m.)	
		SC4	AMP (100μM)
α2β2γ1	145.9 ± 2.1	7.3 ± 0.1	4.4 ± 0.1
α2β2(67-272)γ1	112.6 ± 3.0	6.5 ± 0.1	4.3 ± 0.2

Figure 5. The β2 Subunit Interacts with α2-AID

(A) Sequence alignments between (upper) α1/α2 AIDs, and β1/β2 residues N-terminal to the carbohydrate module (CBM). Secondary structural elements are shown as cylinders for α1 (derived from PDB: 2LTU; magenta) and α2 (derived from our p-α2β1γ1/SC4 structure; orange) and β2 (p-α2β2γ1/SC4; cyan). Predicted secondary structure elements for β1 and β2 are shown as light-green cylinders (http://www.biogem.org/tool/chou-fasman/; Chou and Fasman, 1974).

(B) Close-up view of the α2-AID groove (orange) accommodating a β2 α helix N-terminal to the CBM (cyan). Electron density in this region permits reasonable main-chain, but not side-chain, definition.

(C) Cartoon representation of the exposed α2-AID groove, housing a short helix consisting of β2 residues 60–70, in the p-α2β2γ1/SC4 structure (α2, orange; β2, cyan). The α1-AID from 4RER (green) is superposed for comparison, and conserved residues forming the AID hydrophobic core are highlighted.

(D) α2-AID from the p-α2β2γ1/SC4 complex (orange) superposed to α2-AID from the p-α2β1γ1/SC4 complex (gold).

(E) Cartoon representation of the isolated human α2-AID NMR solution structure (PDB: 2LTU). Hydrophobic core residues are shown as sticks.

(F) Orientations of AIDs in p-α2β2γ1/SC4 (orange) and α2β1γ1/991 (green) complexes, structurally aligned along the kinase large lobe E helix (p-α2β2γ1/SC4 E helix in pink). The AID-interacting β2 helix in our p-α2β2γ1/SC4 structure has been removed for clarity.

(G) *E. coli* expression and CaMKK2-activation of α2β2γ1 (WT) and α2β2(67–272)γ1 (ΔNterm). Purified preparations were immunoblotted as shown.

(H) Dose-response curves for SC4 (0–10 μM) activation of β2-WT and β2-ΔNterm AMPK. n = 4, data presented as mean AMPK activity (fold change relative to untreated ± SEM). Basal activities and maximal fold activation for SC4 and AMP (100 μM) are displayed in the associated table.

adopts an almost identical active conformation regardless of the phosphorylation state of T172 (Xiao et al., 2013; Willows et al., 2017b). This supports our model in which occupancy of AMP/β1-ADaM sites stabilizes the unphosphorylated AMPK activation loop in an active conformation (Scott et al., 2014), but for reasons that are currently unclear this ligand-induced structural restraint does not entirely translate to the β2 isoform.

An interesting feature of our p-α2β2γ1/SC4 structure is significant movement of the α2-AID, most likely resulting from an interaction with a β2 α helix N-terminal to the CBM. The AID is an important AMPK regulatory element that has been proposed to stabilize the kinase domain in an "open" inactive conformation through interactions with both small and large lobes. Autoinhibition is relieved by AMP-induced sequestration of the AID away from the kinase domain, supported by mutagenic studies in which disruption of the AID-kinase domain interaction led to loss of AMP allosteric regulation and reduced susceptibility to pT172 dephosphorylation (Chen et al., 2009), although the latter effect was not observed in a similar study (Li et al., 2015). It is tempting to speculate that the β2-AID interaction might promote enzyme activity by stabilizing AMP-induced sequestration, although our biochemical data using non-myristoylated, bacterial-expressed AMPK does not support this proposal (Figure 5H). However, the β-subunit N terminus inherently contributes to cellular AMPK regulation since prevention of N-myristoylation, or removal of β1 residues 1–63, resulted in hyperactivate AMPK complexes when expressed in mammalian cells (Scott et al., 2008).

Is the interaction specific to α2β2γ1 complexes? Intriguingly, the interacting regions encompass two stretches of isoform sequence heterogeneity that, for the β-subunit, may also

manifest as divergence in secondary structure elements (Figure 5A). On the one hand, this interaction was not observed in our p-α2β1γ1 structure presented here, or structures of AMP/drug-bound, full-length α2β1γ1 in which the AID was resolved (Xiao et al., 2013; Willows et al., 2017b), even though the AID groove is ''accessible'' in all these complexes. On the other hand, deletion of the β N-terminal region and CBM in α2β1γ1 perplexingly abolished AMP suppression of pT172 dephosphorylation (Xiao et al., 2013), suggestive of intramolecular signaling between γ-nucleotide sites and the CBM that might be facilitated by a direct interaction between the β1 N terminus and α2-AID. Whether ADaM-site occupancy is required to stabilize the interaction, and whether the interaction persists in the absence of AMP, are also important questions to address in further investigations.

Off-target tissue effects represent long-appreciated and significant obstacles to clinical use of systemic AMPK activators. Accordingly, the pan-AMPK activator MK-8722 was reported to induce reversible cardiac hypertrophy, although whether this arose as a direct effect of activating cardiac AMPK or represents a secondary complication resulting, for example, from systemic hypertension (Stanton and Dunn, 2017), is unclear. Regardless, despite advances in tissue-specific delivery systems, the challenges facing development of isoform/tissue-specific AMPK activators remain significant. Whereas pan-AMPK activators may have been selected for *in vivo* analysis based on high potency (Cokorinos et al., 2017; Myers et al., 2017), we take the view that isoform selectivity requires at least equal consideration when investigating AMPK-targeting glucose importagogs. We anticipate that structural determinants for SC4 binding presented here will aid development of small-molecule agonists targeting skeletal muscle AMPK α2β2 complexes. Tissue specificity may ultimately be realized with activators of α2β2γ3, found exclusively in skeletal muscle, to avoid potential complications associated with stimulating α2 signaling in the heart. Specifically, β2 potency is conferred by interaction of the core ring-2 4′-nitrogen with the non-conserved β2-D111 (SC4 versus 991). By mutational analysis we showed that the analogous β1 residue N111 is not a major binding determinant for SC4 binding, indicating a therapeutically exploitable point of difference between the two isoforms. Using purified enzyme, SC4 activated all six α2-AMPK complexes, in comparison with only two α1 complexes (Figure 1B). Comparisons of the binding modes of SC4 to β1-AMPK with those of MK-8722 and PF-739 reveal a possible explanation. A striking difference between these compounds is the 2′-mannitol of MK-8722, common to PF-739, in place of the SC4 2′-*o*-toluic acid group (Figure 1A). This allows MK-8722 and PF-739 to make additional backbone contacts with conserved α2 residues F27 and N48 that are absent in the β1/SC4 structure (Figure 4B). These contacts likely strengthen the interaction between the α surface of the ADaM site and PF-739, compared with SC4. Consequently, while promotion of β2 affinity conferred by the 2′-mannitol substituent (PF-739 versus 991) may appear advantageous, this group also promotes activation of all α1-AMPK complexes (SC4 versus MK-8722 and PF-739) and disrupts the path to isoform specificity. Overall, our findings lay the foundations for rational refinement of drug tissue specificity toward skeletal muscle, where the immediate future for AMPK therapeutics appears brightest.

SIGNIFICANCE

Small-molecule activation of β2-AMPK complexes has attracted interest as a strategy to clinically improve glucose homeostasis via skeletal muscle glucose uptake and storage. Principal significance of our results is first provision of structural information of a β2-AMPK/drug complex. 2′-mannitol derivatives, such as MK-8722, are potent pan-AMPK activators that induce off-target effects. Structural comparisons described in this study reveal binding determinants that can be exploited to increase both potency and isoform selectivity, two criteria of AMPK drug development that require equal consideration. We anticipate success in both directions will be afforded by detailed characterization of more β2-AMPK activators. Identification of an interaction between the β-subunit N terminus and α-subunit autoinhibitory domain also opens the door to further studies interrogating mechanisms of AMPK drug action.

STAR★METHODS

Detailed methods are provided in the online version of this paper and include the following:

- KEY RESOURCES TABLE
- CONTACT FOR REAGENT AND RESOURCE SHARING
- EXPERIMENTAL MODEL DETAILS
  - Animals
  - Cell Lines
- METHOD DETAILS
  - Synthesis of SC4
  - 6-Chloro-5-iodo-2-(methylsulfonyl)-3-((2-(trimethylsilyl)ethoxy)methyl)-3*H*-imidazo[4,5-*b*]pyridine (1)
  - Methyl 5-((6-chloro-5-iodo-3-((2-(trimethylsilyl)ethoxy)methyl)-3*H*-imidazo[4,5-*b*]pyridin-2-yl)oxy)-2-methylbenzoate (2)
  - Methyl 5-((6-chloro-5-(2'-hydroxy-[1,1'-biphenyl]-4-yl)-3-((2-(trimethylsilyl)ethoxy)methyl)-3*H*-imidazo[4,5-*b*]pyridin-2-yl)oxy)-2-methylbenzoate (3)
  - 5-((6-Chloro-5-(2'-hydroxy-[1,1'-biphenyl]-4-yl)-3*H*-imidazo[4,5-*b*]pyridin-2-yl)oxy)-2-methylbenzoic acid (SC4)
  - Synthesis of cSC4
  - 6-Chloro-2''-methoxy-4-nitro-[1,1':4',1''-terphenyl]-3-amine (4)
  - 6-Chloro-2''-methoxy-[1,1':4',1''-terphenyl]-3,4-diamine (5)
  - 5-Chloro-6-(2'-methoxy-[1,1'-biphenyl]-4-yl)-1,3-dihydro-2*H*-benzo[*d*]imidazole-2-thione (6)
  - 6-Chloro-5-(2'-methoxy-[1,1'-biphenyl]-4-yl)-2-(methylthio)-1*H*-benzo[*d*]imidazole (7)
  - 6-Chloro-5-(2'-methoxy-[1,1'-biphenyl]-4-yl)-2-(methylsulfonyl)-1*H*-benzo[*d*]imidazole (8)
  - 6-Chloro-5-(2'-methoxy-[1,1'-biphenyl]-4-yl)-2-(methylsulfonyl)-1-((2-(trimethylsilyl)ethoxy) methyl)-1*H*-benzo[*d*]imidazole (9)

- Methyl 5-((6-chloro-5-(2'-methoxy-[1,1'-biphenyl]-4-yl)-1-((2-(trimethylsilyl)ethoxy)methyl)-1*H*-benzo[*d*]imidazol-2-yl)oxy)-2-methylbenzoate (10)
- Methyl 5-((6-chloro-5-(2'-hydroxy-[1,1'-biphenyl]-4-yl)-1*H*-benzo[*d*]imidazol-2-yl)oxy)-2-methylbenzoate (11)
- 5-((6-Chloro-5-(2'-hydroxy-[1,1'-biphenyl]-4-yl)-1*H*-benzo[*d*]imidazol-2-yl)oxy)-2-methylbenzoic acid (cSC4)
- Constructs for Crystallization
- Protein Expression and Purification for Crystallization
- Crystallization
- Protein Expression and Purification for AMPK Assays
- AMPK Activity Assay
- Lentivirus Generation and Expression
- Cell Experiments
- Immunoblotting
- Adenine Nucleotide Measurements
- Mouse Skeletal Muscle Isolation and Glucose Uptake Assay
- Incubation and Electrical Stimulation of Isolated Rat Skeletal Muscles

- QUANTIFICATION AND STATISTICAL ANALYSIS
- DATA AND SOFTWARE AVAILABILITY

SUPPLEMENTAL INFORMATION

Supplemental Information includes four figures and four tables and can be found with this article online at https://doi.org/10.1016/j.chembiol.2018.03.008.

ACKNOWLEDGMENTS

This research was undertaken on the MX2 beamline at the Australian Synchrotron, Victoria, Australia, part of ANSTO, and made use of the ACRF detector. We thank the beamline staff for their assistance. We thank Sandra Galic and Lisa Murray-Segal for assistance with preparation of primary hepatocytes and isolation of mouse muscles. This work was supported by grants from the Australian Research Council (ARC ID:130100988) and the National Health and Medical Research Council (NHMRC ID: 1098459, 1145265). C.G.L. is an EH Flack Fellow and is supported by the Jack Brockhoff foundation (JBF-4206, 2016). M.W.P., B.E.K., and J.B.B. are NHMRC Research Fellows. J.S.O. is an ARC Future Fellow. This study was supported in part by the Victorian Government's Operational Infrastructure Support Program.

AUTHOR CONTRIBUTIONS

K.R.W.N. performed AMPK activity assays and glucose uptake assays. C.G.L. purified and crystallized AMPK constructs. N.X.Y.L. designed, expressed and purified AMPK for crystallization, and performed cellular assays and immunoblotting. A.H., T.A.D., A.J.O., W.J.S. and R.J. performed other experiments. S.J., M.C.C., S.R.W., Y.E.B., and H.H. performed chemical syntheses of SC4 and cSC4. M.W.P., J.W.S., M.H.R., B.E.K., R.C.F., J.B.B., and J.S.O. provided conceptual input. K.R.W.N., C.G.L., and J.S.O. designed the study and wrote the manuscript with contributions from all authors.

DECLARATION OF INTERESTS

The authors declare no competing interests.

Received: November 8, 2017
Revised: January 31, 2018
Accepted: March 19, 2018
Published: April 12, 2018

REFERENCES

Bricogne, G., Blanc, E., Brandl, M., Flensburg, C., Keller, P., Paciorek, P., Roversi, P., Sharff, A., Smart, O., Vonrhein, C., and Womack, T. (2011). BUSTER Version 2.10.0 (Global Phasing Ltd).

Bultot, L., Jensen, T.E., Lai, Y.C., Madsen, A.L., Collodet, C., Kviklyte, S., Deak, M., Yavari, A., Foretz, M., Ghaffari, S., et al. (2016). Benzimidazole derivative small-molecule 991 enhances AMPK activity and glucose uptake induced by AICAR or contraction in skeletal muscle. Am. J. Physiol. Endocrinol. Metab. *311*, E706–E719.

Calabrese, M.F., Rajamohan, F., Harris, M.S., Caspers, N.L., Magyar, R., Withka, J.M., Wang, H., Borzilleri, K.A., Sahasrabudhe, P.V., Hoth, L.R., et al. (2014). Structural basis for AMPK activation: natural and synthetic ligands regulate kinase activity from opposite poles by different molecular mechanisms. Structure *22*, 1161–1172.

Carpio, G.R.A., and Fonseca, V.A. (2014). Update on safety issues related to antihyperglycemic therapy. Diabetes Spectr. *27*, 92–100.

Cameron, K.O., Kung, D.W., Kalgutkar, A.S., Kurumbail, R.G., Miller, R., Salatto, C.T., Ward, J., Withka, J.M., Bhattacharya, S.K., Boehm, M., et al. (2016). Discovery and preclinical characterization of 6-chloro-5-[4-(1-hydroxycyclobutyl)phenyl]-1H-indole-3-carboxylic acid (PF-06409577), a direct activator of adenosine monophosphate-activated protein kinase (AMPK), for the potential treatment of diabetic nephropathy. J. Med. Chem. *59*, 8068–8081.

Chen, L., Jiao, Z.-H., Zheng, L.-S., Zhang, Y.-Y., Xie, S.-T., Wang, Z.-X., and Wu, J.-W. (2009). Structural insight into the autoinhibition mechanism of AMP-activated protein kinase. Nature *459*, 1146–1149.

Chen, L., Xin, F.J., Wang, J., Hu, J., Zhang, Y.Y., Wan, S., Cao, L.S., Lu, C., Li, P., Yan, S.F., et al. (2013). Conserved regulatory elements in AMPK. Nature *498*, E8–E10.

Chen, V.B., Arendall, W.B., 3rd, Headd, J.J., Keedy, D.A., Immormino, R.M., Kapral, G.J., Murray, L.W., Richardson, J.S., and Richardson, D.C. (2010). MolProbity: all-atom structure validation for macromolecular crystallography. Acta Crystallogr. D Biol. Crystallogr. *66*, 12–21.

Cheung, P.C., Salt, I.P., Davies, S.P., Hardie, D.G., and Carling, D. (2000). Characterization of AMP-activated protein kinase gamma-subunit isoforms and their role in AMP binding. Biochem. J. *346*, 659–669.

Chou, P.Y., and Fasman, G.D. (1974). Prediction of protein conformation. Biochemistry *13*, 222–245.

Cokorinos, E.C., Delmore, J., Reyes, A.R., Albuquerque, B., Kjøbsted, R., Jørgensen, N.O., Tran, J.L., Jatkar, A., Cialdea, K., Esquejo, R.M., et al. (2017). Activation of skeletal muscle AMPK promotes glucose disposal and glucose lowering in non-human primates and mice. Cell Metab. *25*, 1147–1159.e10.

Cool, B., Zinker, B., Chiou, W., Kifle, L., Cao, N., Perham, M., Dickinson, R., Adler, A., Gagne, G., Iyengar, R., et al. (2006). Identification and characterization of a small molecule AMPK activator that treats key components of type 2 diabetes and the metabolic syndrome. Cell Metab. *3*, 403–416.

Dite, T.A., Ling, N.X.Y., Scott, J.W., Hoque, A., Galic, S., Parker, B.L., Ngoei, K.R.W., Langendorf, C.G., O'Brien, M.T., Kundu, M., et al. (2017). The autophagy initiator ULK1 sensitizes AMPK to allosteric drugs. Nat. Commun. *8*, 571.

Emsley, P., Lohkamp, B., Scott, W.G., and Cowtan, K. (2010). Features and development of coot. Acta Crystallogr. D Biol. Crystallogr. *66*, 486–501.

Evans, P.R., and Murshudov, G.N. (2013). How good are my data and what is the resolution? Acta Crystallogr. D Biol. Crystallogr. *69*, 1204–1214.

Hanefeld, M. (2007). Pioglitazone and sulfonylureas: effectively treating type 2 diabetes. Int. J. Clin. Pract. Suppl. 20–27.

Hardie, D.G. (2014). AMP-activated protein kinase: a key regulator of energy balance with many roles in human disease. J. Intern. Med. *276*, 543–559.

Hardie, D.G. (2015). AMPK: positive and negative regulation, and its role in whole-body energy homeostasis. Curr. Opin. Cell Biol. *33*, 1–7.

Hawley, S.A., Fullerton, M.D., Ross, F.A., Schertzer, J.D., Chevtzoff, C., Walker, K.J., Peggie, M.W., Zibrova, D., Green, K.A., Mustard, K.J., et al.

(2012). The ancient drug salicylate directly activates AMP-activated protein kinase. Science *336*, 918–922.

Kabsch, W. (2010). XDS. Acta Crystallogr. D Biol. Crystallogr. *66*, 125–132.

Kim, M., Shen, M., Ngoy, S., Karamanlidis, G., Liao, R., and Tian, R. (2012). AMPK isoform expression in the normal and failing hearts. J. Mol. Cell. Cardiol. *52*, 1066–1073.

Kjøbsted, R., Pedersen, A.J., Hingst, J.R., Sabaratnam, R., Birk, J.B., Kristensen, J.M., Højlund, K., and Wojtaszewski, J.F. (2016). Intact regulation of the AMPK signaling network in response to exercise and insulin in skeletal muscle of male patients with Type 2 Diabetes: illumination of AMPK activation in recovery from exercise. Diabetes *65*, 1219–1230.

Lai, Y.C., Kviklyte, S., Vertommen, D., Lantier, L., Foretz, M., Viollet, B., Hallén, S., and Rider, M.H. (2014). A small-molecule benzimidazole derivative that potently activates AMPK to increase glucose transport in skeletal muscle: comparison with effects of contraction and other AMPK activators. Biochem. J. *460*, 363–375.

Langendorf, C.G., and Kemp, B.E. (2015). Choreography of AMPK activation. Cell Res. *25*, 5–6.

Langendorf, C.G., Ngoei, K.R., Scott, J.W., Ling, N.X., Issa, S.M., Gorman, M.A., Parker, M.W., Sakamoto, K., Oakhill, J.S., and Kemp, B.E. (2016). Structural basis of allosteric and synergistic activation of AMPK by furan-2-phosphonic derivative C2 binding. Nat. Commun. *7*, 10912.

Li, X., Wang, L., Zhou, X.E., Ke, J., de Waal, P.W., Gu, X., Tan, M.H., Wang, D., Wu, D., Xu, H.E., et al. (2015). Structural basis of AMPK regulation by adenine nucleotides and glycogen. Cell Res. *25*, 50–66.

McCoy, A.J., Grosse-Kunstleve, R.W., Adams, P.D., Winn, M.D., Storoni, L.C., and Read, R.J. (2007). Phaser crystallographic software. J. Appl. Crystallogr. *40*, 658–674.

Myers, R.W., Guan, H.P., Ehrhart, J., Petrov, A., Prahalada, S., Tozzo, E., Yang, X., Kurtz, M.M., Trujillo, M., Gonzalez Trotter, D., et al. (2017). Systemic pan-AMPK activator MK-8722 improves glucose homeostasis but induces cardiac hypertrophy. Science *357*, 507–511.

O'Neill, H.M. (2013). AMPK and exercise: glucose uptake and insulin sensitivity. Diabetes Metab. J. *37*, 1–21.

Oakhill, J.S., Chen, Z.P., Scott, J.W., Steel, R., Castelli, L.A., Ling, N., Macaulay, S.L., and Kemp, B.E. (2010). beta-Subunit myristoylation is the gatekeeper for initiating metabolic stress sensing by AMP-activated protein kinase (AMPK). Proc. Natl. Acad. Sci. USA *107*, 19237–19241.

Oakhill, J.S., Scott, J.W., and Kemp, B.E. (2012). AMPK functions as an adenylate charge-regulated protein kinase. Trends Endocrinol. Metab. *23*, 125–132.

Schüttelkopf, A.W., and van Aalten, D.M. (2004). PRODRG: a tool for high-throughput crystallography of protein-ligand complexes. Acta Crystallogr. D Biol. Crystallogr. *60*, 1355–1363.

Scott, J.W., van Denderen, B.J.W., Jorgensen, S.B., Honeyman, J.E., Steinberg, G.R., Oakhill, J.S., Iseli, T.J., Koay, A., Gooley, P.R., Stapleton, D., and Kemp, B.E. (2008). Thienopyridone drugs are selective activators of AMP-activated protein kinase beta1-containing complexes. Chem. Biol. *15*, 1220–1230.

Scott, J.W., Ling, N., Issa, S.M., Dite, T.A., O'Brien, M.T., Chen, Z.P., Galic, S., Langendorf, C.G., Steinberg, G.R., Kemp, B.E., and Oakhill, J.S. (2014). Small molecule drug A-769662 and AMP synergistically activate naive AMPK independent of upstream kinase signaling. Chem. Biol. *21*, 619–627.

Scott, J.W., Galic, S., Graham, K.L., Foitzik, R., Ling, N.X., Dite, T.A., Issa, S.M., Langendorf, C.G., Weng, Q.P., Thomas, H.E., et al. (2015). Inhibition of AMP-activated protein kinase at the allosteric drug-binding site promotes islet insulin release. Chem. Biol. *22*, 705–711.

Stanton, T., and Dunn, F.G. (2017). Hypertension, left ventricular hypertrophy, and myocardial ischemia. Med. Clin. North Am. *101*, 29–41.

Steinberg, G.R., O'Neill, H.M., Dzamko, N.L., Galic, S., Naim, T., Koopman, R., Jørgensen, S.B., Honeyman, J., Hewitt, K., Chen, Z.P., et al. (2010). Whole body deletion of AMP-activated protein kinase β2 reduces muscle AMPK activity and exercise capacity. J. Biol. Chem. *285*, 37198–37209.

Stephenne, X., Foretz, M., Taleux, N., van der Zon, G.C., Sokal, E., Hue, L., Viollet, B., and Guigas, B. (2011). Metformin activates AMP-activated protein kinase in primary human hepatocytes by decreasing cellular energy status. Diabetologia *54*, 3101–3110.

Taylor, S.S., Knighton, D.R., Zheng, J., Sowadski, J.M., Gibbs, C.S., and Zoller, M.J. (1993). A template for the protein kinase family. Trends Biochem. Sci. *18*, 84–89.

Thornton, C., Snowden, M.A., and Carling, D. (1998). Identification of a novel AMP-activated protein kinase beta subunit isoform that is highly expressed in skeletal muscle. J. Biol. Chem. *273*, 12443–12450.

Thrasher, J. (2017). Pharmacologic management of type 2 diabetes mellitus: available therapies. Am. J. Cardiol. *120*, S4–S16.

Tonogaki, K., Ino, A., Kojima, E., Katou, M., Iwatsu, M., Tanaka, N., and Fujioka, M.. (2013). Hetero ring-Fused imidazole derivative having AMPK activating effect. US20130184240.

Willows, R., Navaratnam, N., Lima, A., Read, J., and Carling, D. (2017a). Effect of different γ-subunit isoforms on the regulation of AMPK. Biochem. J. *474*, 1741–1754.

Willows, R., Sanders, M.J., Xiao, B., Patel, B.R., Martin, S.R., Read, J., Wilson, J.R., Hubbard, J., Gamblin, S.J., and Carling, D. (2017b). Phosphorylation of AMPK by upstream kinases is required for activity in mammalian cells. Biochem. J. *474*, 3059–3073.

Wojtaszewski, J.F., Birk, J.B., Frøsig, C., Holten, M., Pilegaard, H., and Dela, F. (2005). 5′AMP activated protein kinase expression in human skeletal muscle: effects of strength training and type 2 diabetes. J. Physiol. *564*, 563–573.

Xiao, B., Sanders, M.J., Carmena, D., Bright, N.J., Haire, L.F., Underwood, E., Patel, B.R., Heath, R.B., Walker, P.A., Hallen, S., et al. (2013). Structural basis of AMPK regulation by small molecule activators. Nat. Commun. *4*, 3017.

Zhang, C.S., Hawley, S.A., Zong, Y., Li, M., Wang, Z., Gray, A., Ma, T., Cui, J., Feng, J.W., Zhu, M., et al. (2017). Fructose-1,6-bisphosphate and aldolase mediate glucose sensing by AMPK. Nature *548*, 112–116.

STAR★METHODS

KEY RESOURCES TABLE

REAGENT or RESOURCE	SOURCE	IDENTIFIER
Antibodies		
AMPK α	Cell Signaling Technology	Cat# 2793; RRID: AB_915794
AMPK β	Cell Signaling Technology	Cat# 4150; RRID: AB_10828832
AMPK α-phosphoThr172	Cell Signaling Technology	Cat# 2535; RRID: AB_331250
AMPK β-phosphoSer108	Cell Signaling Technology	Cat# 4181; RRID: AB_2169743
phosphoACC	Cell Signaling Technology	Cat# 3661; RRID: AB_330337
AMPK β1	Abcam	Cat# ab58175; RRID: AB_940250
Anti-rabbit IgG-IR680	LI-COR Biosciences	Cat# LCR-926-68071; RRID: AB_10956166
Anti-mouse IgG-IR800	LI-COR Biosciences	Cat# LCR-926-32210; RRID: AB_621842
Chemicals, Peptides, and Recombinant Proteins		
A-769662	Abcam	Cat# ab120335
Phenformin	Sigma-Aldrich	Cat# P7045
SC-4	This study	N/A
cSC-4	This study	N/A
991	(Lai et al., 2014)	N/A
Staurosporine	Sigma-Aldrich	Cat# S4400
2-deoxy-glucose	Sigma-Aldrich	Cat# D6134
2-deoxy-[1,2-^{3}H]-glucose	PerkinElmer Life Sciences	Cat# NET328250UC
D-[1-^{14}C]-mannitol	PerkinElmer Life Sciences	Cat# NEC314050UC
Fugene HD	Promega	Cat# E2311
S108tide synthetic peptide	(Dite et al., 2017)	N/A
λ-phosphatase	Cell Signaling Technology	Cat# P0753
Flag-CaMKK2	(Oakhill et al., 2010)	N/A
Deposited Data		
α2β1γ1/SC-4 structure	This paper	PDB: 6B1U
α2β2γ1/SC-4 structure	This paper	PDB: 6B2E
Experimental Models: Cell Lines		
COS7	ATCC	CRL-1651
C2C12	ATCC	CRL-1772
HEK293T	ATCC	CRL-3216
Immortalized MEFs WT	(Dite et al., 2017)	N/A
Immortalized MEFs AMPK β1$^{-/-}$/2$^{-/-}$	(Dite et al., 2017)	N/A
Experimental Models: Organisms/Strains		
AMPK β2$^{-/-}$, on C57Bl/6 background	(Steinberg et al., 2010)	N/A
Oligonucleotides		
AMPKα1-D141A ggtggtccataga**gct**ttgaaacctgaaaatg	Sigma-Aldrich	N/A
AMPKβ1-S108A ccccctcaccaga**gcc**cacaataactttgtagc	Sigma-Aldrich	N/A
AMPKβ1-N111A ccagaagccacaat**gcc**tttgtagccatcc	Sigma-Aldrich	N/A
AMPKβ2-S108A ccactgattaag**gcc**cataatgactttgttgc	Sigma-Aldrich	N/A

(*Continued on next page*)

Continued

REAGENT or RESOURCE	SOURCE	IDENTIFIER
AMPKβ2-D111A gattaagagccataat**gcc**tttgttgccatcc	Sigma-Aldrich	N/A
AMPKβ2-ΔNterm ggtaccatggaggactccgtaaagc	Sigma-Aldrich	N/A
Recombinant DNA		
pBSSVD2005 SV40 large-T antigen expression	A gift from David Ron	Addgene #21826
LeGO-iG2 AMPK β2-flag	This study	N/A
psPax2	A gift from Carl Walkley	N/A
pHCMV-EcoEnv	A gift from Carl Walkley	N/A
pET DUET AMPK his-α2/γ1	(Scott et al., 2014)	N/A
pET RSF Duet AMPK β1	(Scott et al., 2014)	N/A
pET RSF Duet AMPK β2	(Scott et al., 2014)	N/A
pET RSF Duet AMPK β2(67-272)	(Scott et al., 2014)	N/A
pDEST27 GST-AMPK α1	(Scott et al., 2014)	N/A
pDEST27 GST-AMPK α2	(Scott et al., 2014)	N/A
pcDNA3 AMPK β1-flag	(Scott et al., 2014)	N/A
pcDNA3 AMPK β2-flag	(Scott et al., 2014)	N/A
pMT2-HA-AMPK γ1	(Scott et al., 2014)	N/A
pMT2-HA-AMPK γ2	(Scott et al., 2014)	N/A
pMT2-HA-AMPK γ3	(Scott et al., 2014)	N/A
Other		
Glutathione-Sepharose 4B	GE Life Sciences	Cat#17075601
Streptavidin-Sepharose	GE Life Sciences	Cat#90100484

CONTACT FOR REAGENT AND RESOURCE SHARING

Further information and requests for resources and reagents should be directed to and will be fulfilled by the Lead Contact: Jonathan Oakhill (joakhill@svi.edu.au).

EXPERIMENTAL MODEL DETAILS

Animals

All animal procedures were approved by St. Vincent's Hospital Animal Ethics Committee or the Ethics Committee of the Life Sciences Sector, Université catholique de Louvain (Male Wistar rats (170-180 g)). Whole body AMPK β2-KO C57BL/6 mice are described previously (Steinberg et al., 2010).

Cell Lines

All cells were cultured in Dulbecco's Modified Eagle's medium (DMEM) containing 10% FBS and 1% penicillin/streptomycin antibiotics, at 37°C with 5% CO_2. COS7 cells and C2C12 myoblasts were from the ATCC (Manassas, VA). C2C12 myoblasts were differentiated into myotubes by culturing in differentiation media (DMEM GlutaMax, supplemented with 2% horse serum and 1% pencillin/streptomycin) for 7 days. MEFs were extracted from WT or homozygous AMPK β1β2 null embryos (days 12–14 post-coitum), generated by crossing homozygous β1 and β2 null mice. WT and AMPK β1/2 double knockout (β1/2-dKO) MEFs were immortalized by Fugene HD-mediated transfection with an SV40 large-T antigen expression construct. (Dite et al., 2017).

METHOD DETAILS

Synthesis of SC4

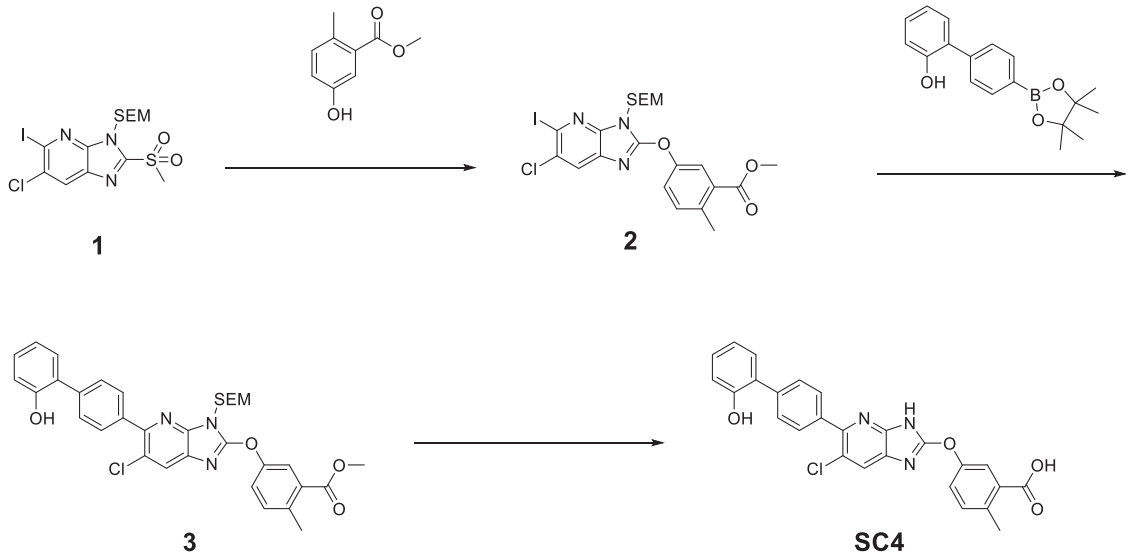

Solvents were of analytical grade: acetonitrile (CH_3CN); ethyl acetate (EtOAc); dichloromethane (DCM); *N*,*N*-dimethylformamide (DMF); methanol (MeOH); tetrahydrofuran (THF). Analytical TLC was performed on silica gel 60 F_{254} pre-coated aluminium sheets (0.25 mm, Merck). Flash column chromatography was carried out with silica gel 60, 0.63–0.20 mm (70–230 mesh, Merck).

^{1}H and ^{13}C NMR spectra were recorded at 400.13, and 100.62 MHz, respectively, on a Bruker Avance III Nanobay spectrometer with BACS 60 sample changer, using solvents from Cambridge Isotope Laboratories. Chemical shifts (δ, ppm) are reported relative to the solvent peak ($CDCl_3$: 7.26 [^{1}H] or 77.16 [^{13}C]; MeOH-d4: 3.31 [^{1}H] or 49 [^{13}C]; DMSO-d6: 2.49 [^{1}H]). Proton resonances are annotated as: chemical shift (ppm), multiplicity (s, singlet; d, doublet; t, triplet; q, quartet; m, multiplet; dd, doublet of doublets; td, triplet of doublets: v br, very broad), coupling constant (*J*, Hz), and number of protons. NH_2 and OH protons are in exchange.

Analytical HPLC was acquired on an Agilent 1260 Infinity analytical HPLC coupled with a G1322A degasser, G1312B binary pump, G1367E high performance autosampler, G4212B diode array detector. Conditions: Zorbax Eclipse Plus C18 Rapid resolution column (4.6 × 100 mm) with UV detection at 254 nm and 214 nm, 30°C; sample was eluted using a gradient of 5–100% of solvent B in solvent A where solvent A: 0.1% aq. TFA, and solvent B: 0.1% TFA in CH_3CN (5 to 100% B [9 min], 100% B [1 min]; 0.5 mL/min).

Preparative HPLC was acquired on an Agilent 1260 Preparative HPLC coupled with a G1361A prep pump, G2260A autosampler, G1315D diode array detector. Conditions: Phenomenex Luna C8 (2) column 100 Å Axia (250 × 21.2 mm; particle size 5 μm) with UV detection at 254 nm and 210 nm, 30°C, flow rate of 10 mL/min. Gradients are as specified in the individual examples.

LCMS was performed on an Agilent 6100 Series Single Quad LCMS coupled with an Agilent 1200 Series HPLC, G1311A quaternary pump, G1329A thermostatted autosampler, and G1314B variable wavelength detector (214 and 254 nm). LC conditions: Phenomenex Luna C8 (2) column (100 Å, 5 μm, 50 × 4.6 mm), 30°C; sample (5 μL) was eluted using a binary gradient (solvent A: 0.1% aq. HCO_2H; solvent B: 0.1% HCO_2H in CH_3CN; 5 to 100% B [10 min], 100% B [10 min]; 0.5 mL/min). MS conditions: quadrupole ion source with multimode-ESI; drying gas temperature, 300°C; vaporizer temperature, 200°C; capillary voltage, 2000 V (positive mode) or 4000 V (negative mode); scan range, 100–1000 *m/z*; step size, 0.1 s over 10 min.

High resolution MS was performed on an Agilent 6224 TOF LCMS coupled to an Agilent 1290 Infinity LC. All data were acquired and reference mass corrected via a dual-spray electrospray ionisation (ESI) source. Each scan or data point on the total ion chromatogram (TIC) is an average of 13,700 transients, producing a spectrum every second. Mass spectra were created by averaging the scans across each peak and subtracting the background from first 10 s of the TIC. Acquisition was performed using the Agilent Mass Hunter Data Acquisition software ver. B.05.00 Build 5.0.5042.2 and analysis was performed using Mass Hunter Qualitative Analysis ver. B.05.00 Build 5.0.519.13. Acquisition parameters: mode, ESI; drying gas flow, 11 L/min; nebuliser pressure, 45 psi; drying gas temperature, 325°C; voltages: capillary, 4000 V; fragmentor, 160 V; skimmer, 65 V; octapole RF, 750 V; scan range, 100–1500 *m/z*; positive ion mode internal reference ions, *m/z* 121.050873 and 922.009798. LC conditions: Agilent Zorbax SB-C18 Rapid Resolution HT (2.1 × 50 mm, 1.8 μm column), 30°C; sample (5 μL) was eluted using a binary gradient (solvent A: 0.1% aq. HCO_2H; solvent B: 0.1% HCO_2H in CH_3CN; 5 to 100% B [3.5 min], 0.5 ml/min).

6-Chloro-5-iodo-2-(methylsulfonyl)-3-((2-(trimethylsilyl)ethoxy)methyl)-3*H*-imidazo[4,5-*b*]pyridine (1)

Title compound was prepared according to literature procedure WO2012116145.

Methyl 5-((6-chloro-5-iodo-3-((2-(trimethylsilyl)ethoxy)methyl)-3*H*-imidazo[4,5-*b*]pyridin-2-yl)oxy)-2-methylbenzoate (2)

To a solution of methyl 5-hydroxy-2-methylbenzoate (122 mg, 0.734 mmol) in DMF (6 mL) was added Cs_2CO_3 (496 mg, 1.53 mmol) and 6-chloro-5-iodo-2-(methylsulfonyl)-3-((2-(trimethylsilyl)ethoxy)methyl)-3*H*-imidazo[4,5-*b*]pyridine (300 mg, 0.612 mmol). The reaction was stirred at room temperature for 2 h. The solvent was removed *in vacuo*, the residue acidified with a 10% a.q. citric acid solution and extracted with EtOAc (×3). The combined organic layers were washed with water, brine, dried ($MgSO_4$) and concentrated *in vacuo* to give the title compound (337 mg, 96% yield). ^{1}H NMR (400 MHz, $CDCl_3$) δ 7.93 (d, *J* = 2.68 Hz, 1H), 7.78 (s, 1H), 7.44 (dd, *J* = 2.70, 8.38 Hz, 1H), 7.35 (dd, *J* = 1.05, 8.38 Hz, 1H), 5.61 (s, 2H), 3.89 (s, 3H), 3.80 – 3.72 (m, 2H), 2.63 (s, 3H), 1.05 – 0.96 (m, 2H), -0.00 (s, 9H).

Methyl 5-((6-chloro-5-(2'-hydroxy-[1,1'-biphenyl]-4-yl)-3-((2-(trimethylsilyl)ethoxy)methyl)-3*H*-imidazo[4,5-*b*]pyridin-2-yl)oxy)-2-methylbenzoate (3)

A microwave vessel under nitrogen was charged with methyl 5-((6-chloro-5-iodo-3-((2-(trimethylsilyl)ethoxy)methyl)-3*H*-imidazo[4,5-*b*]pyridin-2-yl)oxy)-2-methylbenzoate (337 mg, 0.587 mmol), $Pd(PPh_3)_2Cl_2$ (21 mg, 0.0299 mmol), 4'-(4,4,5,5-tetramethyl-1,3,2-dioxaborolan-2-yl)-[1,1'-bipheny]-2-ol (190 mg, 0.642 mmol) and DMF (8 mL). The mixture was bubbled with nitrogen for 5 min and a 1.0M solution of aq. K_2CO_3 (0.875 mL, 0.875 mmol) added. The mixture was bubbled with nitrogen for a further 5 min then heated at 120°C under microwave irradiation for 45 min. The reaction was cooled to room temperature, concentrated, and then partitioned between water and EtOAc. The aq. layer was extracted with EtOAc (×2) and the combined organic phases washed with brine, dried over $MgSO_4$ and the solvent removed *in vacuo* to give the crude material. The product was purified by silica gel chromatography (0-30% EtOAc/petroleum benzine) to afford the title compound (321 mg, 87% yield). ^{1}H NMR (400 MHz, $CDCl_3$) δ 7.97 (d, *J* = 2.69 Hz, 1H), 7.93–7.86 (m, 3H), 7.61–7.56 (m, 2H), 7.48 (dd, *J* = 2.71, 8.33 Hz, 1H), 7.37 (dd, *J* = 1.09, 8.34 Hz, 1H), 7.34–7.27 (m, 2H), 7.06–6.98 (m, 2H), 5.69 (s, 2H), 3.90 (s, 3H), 3.85–3.79 (m, 2H), 2.65 (s, 3H), 1.05–0.98 (m, 2H), -0.03 (s, 9H). LCMS: RT 6.052 min, *m/z* 484.1 $[M\text{-}SEM+H]^+$.

5-((6-Chloro-5-(2'-hydroxy-[1,1'-biphenyl]-4-yl)-3*H*-imidazo[4,5-*b*]pyridin-2-yl)oxy)-2-methylbenzoic acid (SC4)

TBAF (1M in THF) (2.08 mL, 2.08 mmol) was added to a solution of methyl 5-[(6-fluoro-5-(2'-hydroxybiphenyl-4-yl)-1-{(2-(trimethylsilyl)ethoxy]methyl}-l*H*-benzimidazol-2-yl)oxy]-2-methylbenzoate (321 mg, 0.521 mmol) in THF (10 mL). The reaction was heated at 80°C for 6 h. The volatiles were removed *in vacuo* and the resultant residue dissolved in MeOH (6 mL) and a 2.5M aq. sol. of NaOH (2 mL). The solution was heated at 70°C for 30 min after which the volatiles were removed *in vacuo*, the residue taken up in 10 mL water and extracted with EtOAc. The combined organic layers were washed with brine, dried over $MgSO_4$ and the solvent removed *in vacuo*. The resultant crude material was purified by silica gel chromatography (0-100% EtOAc/petroleum benzine) to afford the title compound (SC4) (70 mg, 28% yield, > 95% pure as judged by ^{1}H-NMR) as an off-white solid. Characterisation by ^{1}H NMR was in agreement with the literature values. This compound has been synthesised previously in the literature: compound C-4, WO2012033149 A1.

Synthesis of cSC4

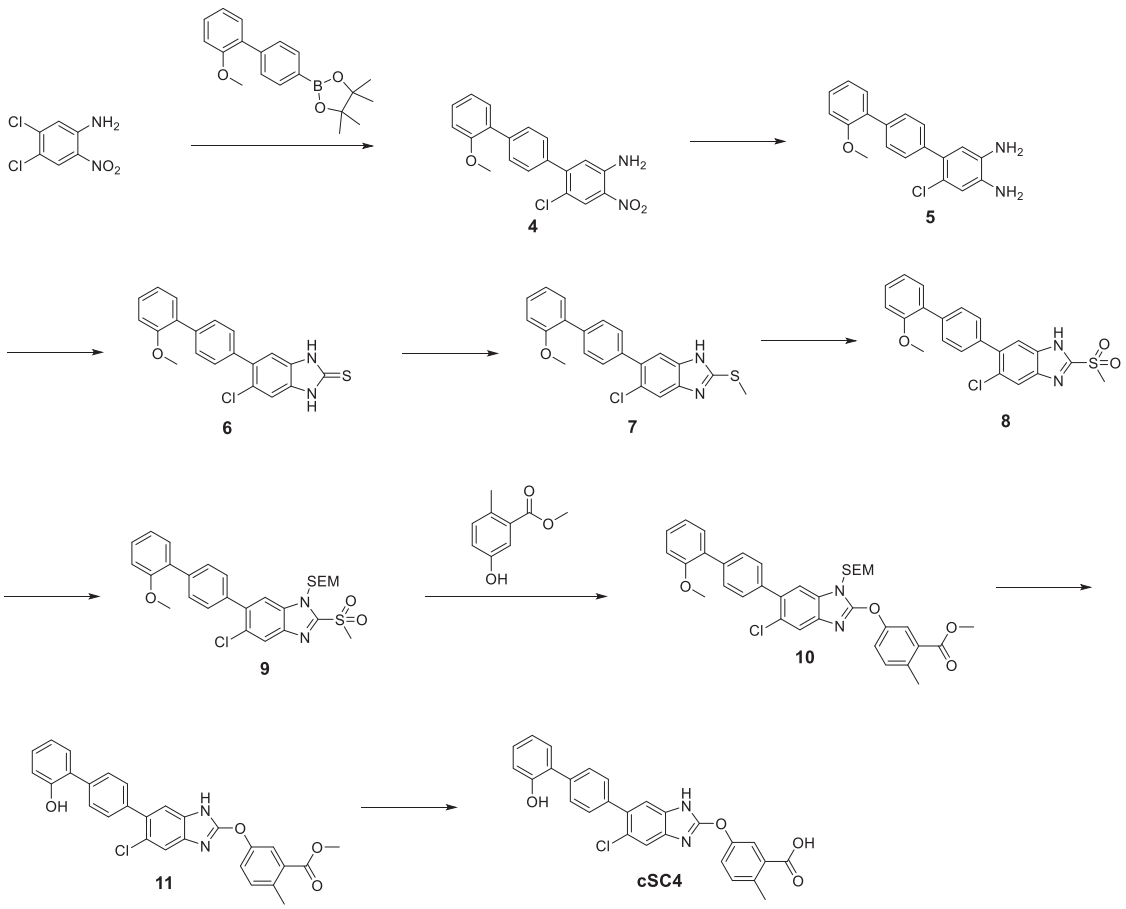

6-Chloro-2''-methoxy-4-nitro-[1,1':4',1''-terphenyl]-3-amine (4)

4,5-Dichloro-2-nitroaniline (529 mg, 2.55 mmol) and 2'-methoxybiphenyl-4-boronic acid pinacol ester (0.71 g, 2.3 mmol) were dissolved in 3 mL of 3:1 1,4-dioxane/water mixture. To this solution K_2CO_3 (1.0 g, 7.7 mmol) and TBAB (82 mg, 0.26 mmol) were added and the solution was degassed for 15 min. A catalytic amount of $Pd(dppf)Cl_2$ (93 mg, 0.13 mmol) was then added and the reaction mixture irradiated using a microwave reactor at 130°C for 3 h. After completion of the reaction as indicated by TLC analysis, the reaction mixture was filtered through celite and then evaporated to dryness. Purification was performed by flash chromatography (5% EtOAc/petroleum spirits) to obtain the title compound as a yellow solid (519 mg, 63%). ^{1}H NMR (400 MHz, $CDCl_3$) δ 8.28 (s, 1H), 7.67–7.59 (m, 2H), 7.51–7.45 (m, 2H), 7.45–7.40 (m, 1H), 7.40–7.33 (m, 2H), 7.29 (m, 1H), 7.06 (td, *J* = 7.5, 1.0 Hz, 1H), 7.04–7.00 (m, 1H), 6.85 (s, 1H), 3.85 (s, 3H); ^{13}C NMR (101 MHz, $CDCl_3$) δ 156.7, 148.1, 143.1, 139.3, 136.0, 131.0, 130.8, 129.5, 129.2, 128.8, 128.4, 127.0, 121.1, 120.8, 115.1, 111.5, 55.7; HPLC: RT 8.01 min > 99% purity at 254 nm; LCMS: *m/z* 354.8 $[M+H]^+$; HRMS: *m/z* 355.0844 $[M+H]^+$, found *m/z* 355.0834

6-Chloro-2''-methoxy-[1,1':4',1''-terphenyl]-3,4-diamine (5)

6-Chloro-2''-methoxy-4-nitro-[1,1':4',1''-terphenyl]-3-amine (519 mg, 1.46 mmol) was dissolved in 1 mL ethanol and treated with tin(II) chloride dihydrate (1.3 g, 5.9 mmol). The reaction mixture was then heated to 70°C for 24 h. After completion of reaction as indicated by TLC analysis, KF (1 g, 17.2 mmol) in 2.5 mL of water was added and the solution stirred for 30 min. The reaction was then quenched with water and washed with EtOAc (×3). The combined organic layers were then dried with $MgSO_4$, filtered through a pad of silica and evaporated to dryness to yield the title compound as a yellow oil (426 mg, 89%). ^{1}H NMR (400 MHz, $CDCl_3$) δ 7.59–7.54 (m, 2H), 7.49–7.44 (m, 2H), 7.44–7.27 (m, 6H), 7.07–7.03 (m, 1H), 7.02 (m, 1H), 6.82 (s, 1H), 6.75 (s, 1H), 3.84

(s, 3H); ^{13}C NMR (101 MHz, $CDCl_3$) δ 158.3, 156.5, 156.5, 148.1, 130.9, 130.9, 129.2, 129.1, 129.1, 128.8, 128.7, 128.6, 123.9, 121.0, 120.9, 111.3, 55.6; HPLC: RT 6.71 min > 85% purity at 254 nm; LCMS: *m/z* 324.9 $[M+H]^+$.

5-Chloro-6-(2'-methoxy-[1,1'-biphenyl]-4-yl)-1,3-dihydro-2*H*-benzo[*d*]imidazole-2-thione (6)

To a mixture of 6-chloro-2''-methoxy-[1,1':4',1''-terphenyl]-3,4-diamine (100 mg, 0.3 mmol) dissolved in 0.5 mL ethanol, a solution of KOH (21 mg, 0.37 mmol) dissolved in 0.1 mL water was added, followed by addition of CS_2 (22 μL, 0.37 mmol). The solution was then refluxed for 5 h. After completion of the reaction as indicated by TLC analysis, the solution was carefully neutralised with 1M aq. HCl and then washed with EtOAc (×3). The combined organic layers were then washed with brine, dried with $MgSO_4$, filtered and evaporated to dryness. Purification was performed by flash chromatography (10% EtOAc/petroleum spirits) to obtain the title compound as a white solid (50.1 mg, 45%). ^{1}H NMR (400 MHz, $CDCl_3$) δ 7.62 (m, 2H), 7.50 (m, 2H), 7.43–7.31 (m, 3H), 7.11–6.92 (m, 3H), 3.85 (s, 3H); HPLC: RT 6.94 min > 98% purity at 254 nm; LCMS: *m/z* 364.8 $[M-H]^-$; HRMS: *m/z* 367.0666 $[M+H]^+$, found *m/z* 367.0678.

6-Chloro-5-(2'-methoxy-[1,1'-biphenyl]-4-yl)-2-(methylthio)-1*H*-benzo[*d*]imidazole (7)

To 5-chloro-6-(2'-methoxy-[1,1'-biphenyl]-4-yl)-1,3-dihydro-2*H*-benzo[*d*]imidazole-2-thione (0.28 g, 0.75 mmol) dissolved in 5 mL acetone at 0°C, was added K_2CO_3 (52 mg, 0.38 mmol) and iodomethane (24 μL, 0.38 mmol). The reaction was then stirred for 2 h at room temperature. After completion of the reaction as indicated by TLC analysis, the reaction mixture was washed with EtOAc (×3). The combined organic layer was then washed with water, dried with $MgSO_4$, filtered and evaporated to dryness to obtain the crude product as a yellow oil (270 mg, 95%) which was directly used for the next step without further purification. ^{1}H NMR (400 MHz, $CDCl_3$) δ 9.14 (s, 1H), 7.64–7.58 (m, 2H), 7.55–7.48 (m, 2H), 7.44–7.29 (m, 3H), 7.06 (m, 1H), 7.01 (m, 1H), 3.86 (s, 3H), 2.83–2.79 (m, 3H); ^{13}C NMR (101 MHz, $CDCl_3$) δ 156.5, 153.3, 138.5, 137.5, 134.8, 131.3, 131.0, 130.9, 130.2, 129.6, 129.5, 129.1, 129.1, 128.7, 126.7, 120.9, 111.3, 55.6, 14.7; HPLC: RT 6.8 min > 84% purity at 254 nm; LCMS: *m/z* 380.8 $[M+H]^+$; HRMS: *m/z* 381.0823 $[M+H]^+$, found *m/z* 381.0821.

6-Chloro-5-(2'-methoxy-[1,1'-biphenyl]-4-yl)-2-(methylsulfonyl)-1*H*-benzo[*d*]imidazole (8)

mCPBA (245 mg, 1.42 mmol) was added to a solution of 6-chloro-5-(2'-methoxy-[1,1'-biphenyl]-4-yl)-2-(methylthio)-1*H*-benzo[*d*]imidazole (0.27 g, 0.71 mmol) in 5 mL DCM and the reaction stirred at room temperature for 10 min. The reaction mixture was then washed with 10% aq. $NaHCO_3$ solution, dried with $MgSO_4$, filtered and evaporated to dryness. Purification was performed by flash chromatography (25% EtOAc/petroleum spirits) to obtain the title compound as a white solid (110 mg, 37%). ^{1}H NMR (400 MHz, $CDCl_3$) δ 10.37 (d, *J* = 18.7 Hz, 1H), 7.97 (d, *J* = 46.5 Hz, 1H), 7.77–7.56 (m, 3H), 7.55–7.47 (m, 2H), 7.41 (dd, *J* = 7.5, 1.6 Hz, 1H), 7.36 (m, 1H), 7.10–6.99 (m, 2H), 3.87 (s, 3H), 3.44 (s, 3H); HPLC: RT 7.11 min > 99% purity at 254 nm; LCMS: *m/z* 410.9 $[M-H]^-$; HRMS: *m/z* 413.0721 $[M+H]^+$, found *m/z* 413.0719.

6-Chloro-5-(2'-methoxy-[1,1'-biphenyl]-4-yl)-2-(methylsulfonyl)-1-((2-(trimethylsilyl)ethoxy) methyl)-1*H*-benzo[*d*] imidazole (9)

Et_3N (67 μL, 0.48 mmol) and SEMCl (56 μL, 0.31 mmol) were successively added to 6-chloro-5-(2'-methoxy-[1,1'-biphenyl]-4-yl)-2-(methylsulfonyl)-1*H*-benzo[*d*]imidazole (100 mg, 0.24 mmol) in 1 mL THF. The reaction was stirred for 1 h at room temperature and then quenched with water. The aq. layer was extracted with EtOAc (×3) and then the combined organic layers were washed with 2M HCl, brine, dried with $MgSO_4$, filtered and evaporated to dryness. Purification was performed by flash chromatography (15-50% EtOAc/petroleum spirits) to obtain the title compound as a clear oil (67 mg, 52%). ^{1}H NMR (400 MHz, $CDCl_3$) δ 7.93 (d, *J* = 46.5 Hz, 1H), 7.68 (m, 3H), 7.55–7.47 (m, 2H), 7.41 (dt, *J* = 7.5, 1.9 Hz, 1H), 7.39–7.32 (m, 1H), 7.07 (m, 1H), 7.04–6.98 (m, 1H), 5.92 (d, *J* = 6.2 Hz, 2H), 3.87 (d, *J* = 1.3 Hz, 3H), 3.74–3.63 (m, 2H), 3.55 (s, 3H), 0.95 (m, 2H), 0.05– -0.12 (m, 9H); HPLC: RT 9.15 min > 93% purity at 254 nm; LCMS: *m/z* 542.8 $[M+H]^+$; HRMS: *m/z* 543.1535 $[M+H]^+$, found *m/z* 543.1529.

Methyl 5-((6-chloro-5-(2'-methoxy-[1,1'-biphenyl]-4-yl)-1-((2-(trimethylsilyl)ethoxy)methyl)-1*H*-benzo[*d*]imidazol-2-yl)oxy)-2-methylbenzoate (10)

6-Chloro-5-(2'-methoxy-[1,1'-biphenyl]-4-yl)-2-(methylsulfonyl)-1-((2-(trimethylsilyl)ethoxy) methyl)-1*H*-benzo[*d*]imidazole (67 mg, 0.12 mmol) and methyl 5-hydroxy-2-methylbenzoate (31 mg, 0.19 mmol) were dissolved in 1 mL DMF to which K_2CO_3 (66 mg, 0.48 mmol) was added and the reaction stirred at room temperature for 12 h. After completion of reaction as indicated by TLC analysis, the DMF was evaporated off and the residue was acidified with 1M aq. HCl. The aq. layer was washed with EtOAc (×3), combined organic layer washed with water and brine, dried with $MgSO_4$, filtered and evaporated to dryness. Purification was performed by flash chromatography (15% EtOAc/petroleum spirits) to obtain the title compound as a yellow oil (69 mg, 92%). ^{1}H NMR (400 MHz, $CDCl_3$) δ 7.96–7.90 (m, 1H), 7.70–7.57 (m, 3H), 7.57–7.44 (m, 3H), 7.45–7.30 (m, 4H), 7.11–6.99 (m, 2H), 5.54 (d, *J* = 6.8 Hz, 2H), 3.88 (dd, *J* = 13.6, 3.5 Hz, 6H), 3.69 (dd, *J* = 16.5, 8.8 Hz, 2H), 2.64 (d, *J* = 3.4 Hz, 3H), 1.05–0.93 (m, 2H), 0.08–-0.06 (m, 9H); HPLC: RT 9.94 min > 99% purity at 254 nm; HRMS: *m/z* 629.2233 $[M+H]^+$, found *m/z* 629.2236.

Methyl 5-((6-chloro-5-(2'-hydroxy-[1,1'-biphenyl]-4-yl)-1*H*-benzo[*d*]imidazol-2-yl)oxy)-2-methylbenzoate (11)

To a -78°C cooled solution of methyl 5-((6-chloro-5-(2'-methoxy-[1,1'-biphenyl]-4-yl)-1-((2-(trimethylsilyl)ethoxy)methyl)-1*H*-benzo[*d*]imidazol-2-yl)oxy)-2-methylbenzoate (28 mg, 0.044 mmol) in 3 mL DCM was added 1M BBr_3 in DCM (2 mL, 2 mmol) dropwise. The reaction was stirred for 12 h allowing it to slowly warm up to room temperature. MeOH was carefully added to quench the

reaction and the reaction mixture evaporated to dryness. DCM was then added and the mixture filtered to obtain the product as an off-white solid (14 mg, 65%). ^{1}H NMR (400 MHz, MeOD) δ 8.19–7.86 (m, 2H), 7.77–7.43 (m, 6H), 7.33 (m, 1H), 7.22–7.14 (m, 1H), 6.98–6.85 (m, 2H), 6.38 (d, *J* = 3.9 Hz, 1H), 3.97–3.90 (m, 3H), 2.71–2.61 (m, 3H); LCMS: *m/z* 484.7 $[M+H]^+$.

5-((6-Chloro-5-(2'-hydroxy-[1,1'-biphenyl]-4-yl)-1*H*-benzo[*d*]imidazol-2-yl)oxy)-2-methylbenzoic acid (cSC4)

To a stirred solution of methyl 5-((6-chloro-5-(2'-hydroxy-[1,1'-biphenyl]-4-yl)-1*H*-benzo[*d*]imidazol-2-yl)oxy)-2-methylbenzoate (14 mg, 0.02 mmol) in 2 mL MeOH was added 2 mL 2M aq. NaOH solution and the reaction stirred at 45°C for 12 h. After completion of the reaction as indicated by TLC analysis, the reaction mixture was neutralised to pH 7 using 6M aq. HCl solution and then evaporated to remove MeOH. The residue was washed with EtOAc (×3), dried with $MgSO_4$, filtered and evaporated to dryness. Purification was performed by high performance liquid chromatography, eluting with 30-100% CH_3CN/water with 0.1% TFA, to obtain the title compound as an off-white solid (2.5 mg, 26%). ^{1}H NMR (400 MHz, MeOD) δ 7.89 (m, 1H), 7.63 (m, 3H), 7.47–7.44 (m, 3H), 7.32 (m, 2H), 7.19–7.13 (m, 2H), 6.91 (m, 3H), 2.63 (s, 3H); HPLC: RT 6.59 min > 83% purity at 254 nm; LCMS: *m/z* 470.8 $[M+H]^+$; HRMS: *m/z* 471.1106 $[M+H]^+$, found *m/z* 471.1113.

Constructs for Crystallization

Heterotrimeric human AMPK His_6-α2β1γ1 and His_6-α2β2γ1 were expressed in *E. coli* strain Rosetta (DE3) using the pETDuet™-1 expression system (Novagen) (Scott et al., 2014). cDNAs for α2 and γ1 were sequentially inserted into pETDuet™-1 multiple cloning sites (MCS) 1 (BamH1/Not1) and 2 (MfeI/XhoI), respectively, resulting in incorporation of an N-terminal hexahistidine tag onto α2. cDNAs for β1 or β2 was inserted into pRSFDuet™-1 MCS1 (NcoI/BamHI). All expression constructs were sequence verified.

Protein Expression and Purification for Crystallization

Expression cultures were grown in Luria-Bertani broth and induced at 16°C with 0.25 mM isopropyl β-D-1-thiogalactopyranoside, prior to overnight incubation. Cells were lysed using a precooled EmulsiFlex-C5 homogenizer (Avestin) and AMPK purified using Nickel Sepharose and size exclusion chromatography as described previously (Langendorf et al., 2016). Phosphorylated AMPK was generated by incubation with CaMKK2 (expressed in Sf21 cells as a C-terminal FLAG fusion, (Oakhill et al., 2010)), in the presence of 2.5 mM $MgCl_2$, 0.5 mM ATP and 0.5 mM AMP (1 h, 22°C). Protein was re-purified using size exclusion chromatography, concentrated to ~10 mg/ml and flash frozen in liquid nitrogen prior to storage at -80°C (storage buffer: 50 mM Tris.HCl, pH 8.0, 150 mM NaCl, 2 mM Tris(2-carboxyethyl)phosphine hydrochloride).

Crystallization

Full-length, phosphorylated α2β1γ1 (4 mg/ml) was mixed with a three-fold molar excess of AMP and two-fold excess of S108tide (NH_2-KLPLTRSHNNFVARRR-COOH) (Dite et al., 2017) and a 1:1 molar ratio of staurosporine and SC4. α2β1γ1 crystals were grown following the described method (Xiao et al., 2013; Langendorf et al., 2016). Protein/compound mixture was added 1:1 at 22°C with a reservoir solution containing 8% PEG 3350, 0.1 M $MgCl_2$, 1.0% glucose, 0.001% cocamidopropyl betaine and 0.1 M imidazole (pH 6.2), and incubated at 4°C for 1-2 weeks. Protein crystals were incubated with reservoir solution containing an additional 5% glycerol, 5% PEG 400, 5% MPD, 5% sucrose, 5% sorbitol and 5% ethylene glycol for 1-2 min before flash-cooling in liquid nitrogen. Phosphorylated α2β2γ1 protein was prepared as per α2β1γ1. Crystals were grown by equally adding protein/compound mixture at 22°C with a reservoir solution containing 6-8% PEG 3350, 0.1 M $MgCl_2$, 0.001% cocamidopropyl betaine and 0.1 M imidazole (pH 6.0), and incubating at 4°C for 1-2 weeks. Individual protein crystals were then transferred to a new crystallisation drop containing identical reservoir solution, except the precipitant concentration was reduced to 4-5% PEG 3350, and incubated at 4°C for a further 1-2 weeks. Protein crystals were incubated with reservoir solution containing an additional 30% sorbitol for 2 min before flash-cooling in liquid nitrogen. Data were collected on the MX2 beamline at the Australian Synchrotron, part of ANSTO. Data were processed and integrated using XDS (Kabsch, 2010) and scaled using AIMLESS from the CCP4 suite (Evans and Murshudov, 2013). The structure was solved by molecular replacement using Phaser from the CCP4 suite (McCoy et al., 2007) and 4CFE (Xiao et al., 2013) as the search model. Iterative rounds of model building and refinement were performed using Coot (Emsley et al., 2010) and Buster (https://www.globalphasing.com/buster/) (Bricogne et al., 2011) respectively. SC4 molecular coordinates and restraints were generated using the PRODRG web-server (Schüttelkopf and van Aalten, 2004). Omit maps were calculated using Buster (Bricogne et al., 2011). Structure validation and protein-SC4 interactions was performed using Molprobity (Chen et al., 2010), figures were created using Pymol (https://www.pymol.org/).

Protein Expression and Purification for AMPK Assays

Heterotrimeric AMPK was expressed in COS7 mammalian cells (Scott et al., 2014). For AMPK complex screening, 12 AMPK heterotrimeric combinations (α1β1γ1 through α2β2γ3) were expressed in COS7 cells using transient transfection with FuGENE HD, according to manufacturer's protocol (Promega). Transfected AMPK heterotrimers consisted of N-terminal GST-tagged α1 or α2 (pDEST27 expression vector), C-terminal FLAG-tagged β1 or β2 (pcDNA3.1 expression vector) and N-terminal HA-tagged γ1, γ2 or γ3 (pMT2 expression vector). AMPK complexes from prepared COS7 lysates were purified using glutathione Sepharose. Synergy experiments were conducted using λ-phosphatase treated AMPK from COS7 cells. Briefly, AMPK GST-α1/FLAG-β1/HA-γ1 or GST-α2/FLAG-β2/HA-γ1 complexes were immobilized on Glutathione Sepharose 4B, incubated on a rotating wheel with λ-phosphatase for 1 h at 22°C (in Buffer A: 50 mM HEPES pH 7.4, 150 mM NaCl, 10% glycerol, 0.01% Tween-20, supplemented with 2 mM

$MnCl_2$), followed by repeated washes in Buffer A and elution in Buffer A supplemented with 20 mM reduced glutathione. Lack of AMPK phosphorylation on α-T172 and β-S108 was confirmed by immunoblot, prior to assay.

Heterotrimeric α2β2ΔNtermγ1 was generated by inserting cDNA for truncated β2 subunit (residues 67-272) into pRSFDuet^{TM}-1 MCS1 (NcoI/BamHI) and expressing in *E.coli*, as described above. Preparations were activated by CaMKK2 treatment during purification, as described above, prior to activity assay.

AMPK Activity Assay

AMPK activity assays using radiolabelled [γ-^{32}P]-ATP were conducted as described previously (Scott et al., 2008). AMPK heterotrimers purified from COS7 cells were immobilized on glutathione Sepharose as above and washed extensively with wash buffer (50 mM HEPES pH 7.4, 150 mM NaCl, 10% glycerol, 1 mM DTT and 0.1% Tween-20) prior to kinase reaction. Assays were conducted in the presence of 100 μM SAMS synthetic peptide (sequence: NH_2-HMRSAMSGLHLVKRR-COOH), 5 mM $MgCl_2$, 200 μM [γ-^{32}P] ATP for 10 min at 30°C ± SC4 or AMP (100 μM). For synergy experiments using dephosphorylated AMPK α1β1γ1 and α2β2γ1, additional ligand control A769662 (20 μM) was included. Phosphotransferase activity was quenched by spotting onto P81 phosphocellulose paper (Whatman, GE Healthcare) followed by repeated washes in 1% phosphoric acid. ^{32}P transfer to the SAMS peptide was quantified by liquid scintillation counting (Perkin Elmer).

Lentivirus Generation and Expression

Lentivirus expression constructs LeGO-iG2, second generation viral packaging vector psPax2 and ecotropic envelope vector pHCMV-EcoEnv were gifts from Carl Walkley (St Vincent's Institute of Medical Research). cDNA for human AMPK β2 was generated with C-terminal FLAG-tag and cloned into LeGO-iG2 using BamHI/NotI restriction sites. Ecotropic lentivirus was generated by transient transfection of HEK293T cells using calcium phosphate (Dite et al., 2017). 1 day prior to transfection, 2–2.5 × 10^6 HEK293T cells were seeded per 10 cm culture dish. LeGO-iG2, psPax2 and pHCMV-EcoEnv plasmids (10 μg, 6.3 μg and 3.8 μg per 10 cm culture dish, respectively) were mixed together with 2 M CaCl2 solution (244 mM final concentration in 500 μl). The DNA/CaCl2 solution was added drop-wise, with vortexing, into 500 μl of 2xHEPES-buffered saline, pH 7.06. After 20 min incubation at RT, the mixture was transferred dropwise onto HEK293T cell culture and incubated. Within 16 h of transfection, cell were washed with phosphate-buffered saline (PBS) and replaced with 6 ml fresh media. The lentivirus-containing supernatant was harvested after 48 and 72 h posttransfection and stored at −80°C.

iMEFs were transduced in 6-well plates by spinoculation. Briefly, 1 day prior to transduction, 0.5 × 10^5 cells per well in a 6-well plate were seeded in 2 ml media. 200 μl lentivirus supernatant in the presence of 8 μg/ml polybrene in 2 ml media was spun for 98 min at 25°C, 1100×g (Heraeus Megafuge 2.0 R). Lentivirus containing media was replaced with an equal volume of fresh media after 24 h. 72 hours post-transduction, iMEFs were incubated with fresh media for 1 h and treated as indicated. Cells were harvested by washing with ice-cold PBS, followed by rapid lysis *in situ* using 100 μl ice-cold lysis buffer (50mM Tris.HCl (pH 7.4), 150mM NaCl, 50mM NaF, 1mM sodium pyrophosphate, 1mM EDTA, 1mM EGTA, 1mM dithiothreitol, 1% (v/v) Triton X-100 and protease inhibitors), and cellular debris was removed by centrifugation.

Cell Experiments

Differentiated C2C12 myotubes were pre-treated with fresh DMEM GlutaMax for 3 hours, prior to incubation with SC4 (0.03–3 μM) or phenformin (2 mM) for 1 h. β1/2 dKO iMEFs were incubated with fresh DMEM for 3 h prior to incubation with SC4 (1–10 μM) or phenformin (2 mM) for 1 h. All cells were washed with ice-cold phosphate buffered saline (PBS) and harvested by rapid lysis using 150 μl ice-cold lysis buffer (50 mM Tris.HCl pH 7.4, 150 mM NaCl, 50 mM NaF, 1 mM sodium pyrophosphate, 1 mM EDTA, 1 mM EGTA, 1 mM DTT, 1% Triton X-100 and cOmplete protease inhibitor cocktail). Lysates were clarified by centrifugation (14,000 rpm; 3 min; 4°C) and flash frozen in liquid N_2 until processed.

Immunoblotting

Samples were separated by SDS-PAGE on a 12% gel (7% for ACC, previously enriched using streptavidin-Sepharose (Scott et al., 2014)) and transferred to Immobilon-FL PVDF membrane (EMD Millipore). Membrane was blocked in PBS + 0.1% Tween-20 (PBST) with 2% non-fat milk for 30 min at 22°C, then incubated for either 1 h or overnight with 1° antibodies (dilutions in PBST). After washes with PBST, membranes were incubated with anti-rabbit or anti-mouse IgG 2° antibodies, fluorescently-labelled with IR680 or IR800 dye, for 1 h. Immunoreactive bands were visualised on an Odyssey® Infrared Imaging System with densitometry analyses determined using ImageStudioLite software (LI-COR Biosciences).

Adenine Nucleotide Measurements

Adenine nucleotides were extracted from cells with perchloric acid (Scott et al., 2015). Relative concentrations were measured by LC-MS on a QTRAP® 5500 mass spectrometer (AB-SCIEX).

Mouse Skeletal Muscle Isolation and Glucose Uptake Assay

Soleus and extensor digitorum longus (EDL) were isolated from anaesthetized mice (mixture of xylazine (20 mg/kg) and ketamine (100 mg/kg) in a volume of 10 μl/g body weight), transferred to glass vials containing 2 ml of basal buffer (Krebs-Henseleit bicarbonate buffer pH 7.4 supplemented with 2 mM pyruvate, 8 mM mannitol and 0.1% BSA; gassed with 95% O_2 + 5% CO_2) and pre-incubated

in a shaking incubator at 30°C for 10 min for recovery (Steinberg et al., 2010). Muscles were incubated in basal buffer ± SC4 (10 μM)) for 30 minutes, in a shaking incubator at 30°C with a gas phase of 95% O_2 + 5% CO_2. 2-deoxy-D-glucose (2DG) uptake was measured over 20 min by replacing basal buffer with glucose uptake buffer (basal buffer supplemented with 1.5 μCi/ml 2-deoxy-[1,2-^{3}H]-glucose and 0.2 μCi/ml D-[1-^{14}C]-mannitol ± SC4 (10 μM)). Muscles were washed in ice-cold PBS, homogenized in 300 μl ice-cold lysis buffer (50 mM HEPES pH 7.4, 150 mM NaCl, 5 mM EDTA, 100 mM NaF, 1 mM Na_3VO_4, 10 mM sodium pyrophosphate, 250 mM sucrose, 1% Triton X-100 and cOmplete protease inhibitor cocktail) using an electrical homogenizer, and clarified by centrifugation (14,000 rpm, 5 min, 4°C). The incorporated radioactivity in muscle extracts (100 μl) was measured by liquid scintillation counting (Perkin Elmer), and calculated as the accumulation of intracellular 2-deoxy-[1,2-^{3}H]-glucose.

Incubation and Electrical Stimulation of Isolated Rat Skeletal Muscles

Anesthetized rats were euthanized by cervical dislocation and epitrochlearis muscles were rapidly removed and mounted on an incubation apparatus. Epitrochlearis muscles were incubated (Lai et al., 2014) in the presence of 991 (5 μM), SC4 (1 μM and 2 μM) or vehicle (0.1% DMSO) for 60 min with or without contraction induced by electrical stimulation (200 ms trains delivered every 5 s at 100 Hz and 30 V) for 30 min.

QUANTIFICATION AND STATISTICAL ANALYSIS

Data analyses were performed using GraphPad Prism 7 software. Results from replicate experiments (n) were expressed as means ± standard error (s.e.m.). All statistical tests were performed using one-way or two-way analysis of variance (ANOVA), or unpaired two-tailed Student's *t* test, where appropriate. Values for EC_{50} and maximum response were calculated from a non-linear regression fit using Prism 7 software.

DATA AND SOFTWARE AVAILABILITY

The co-ordinates for SC-4 complexed to α2β1γ1 and α2β2γ1 have been deposited in the PDB under ID codes 6B1U and 6B2E, respectively.